CentraleSupelec - Synchrotron project

Beamlight design: X-ray angiography

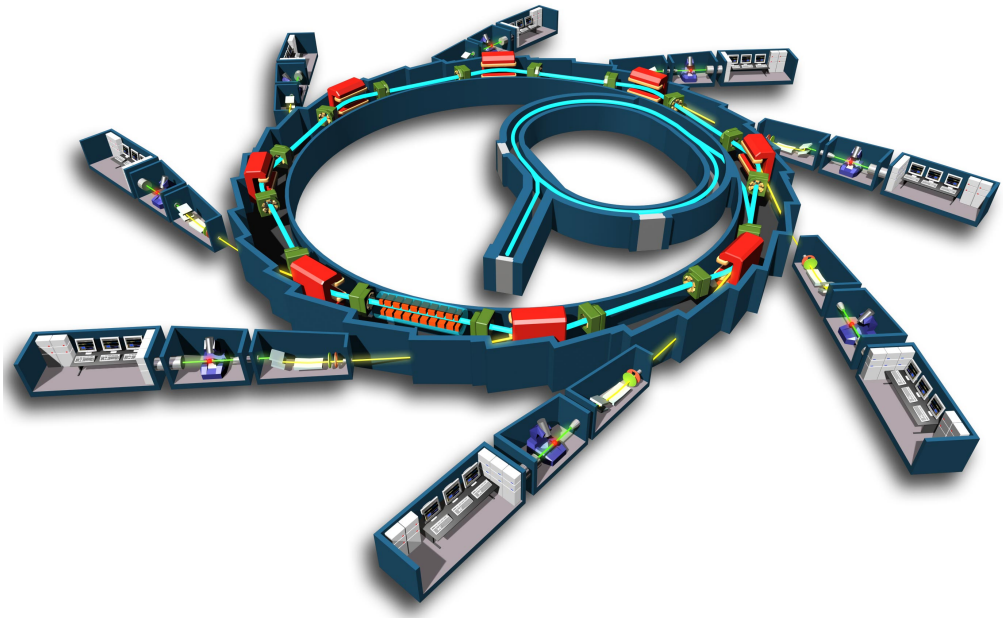

- Beamline Manager: *P.* d'Halluin
- Beam Generation: *B.* De Bruyne, *A.* Remaki, *P.* Nery, *C.* Cozzarini, *T.* Kaimakamis
- Front End: *M.* Banet-Rivet, *F.* Gardères, *A.* Goldani R. Peixoto, *P.* Martin, *P.* Senty
- Beam Conditioning: *G.* Villaret, *C.* Daveau, *A.* Klopocki, *E.* De Agustin, *L.* Nouvelle
- Sample Environment: *P.* Gaudin, *T.* Ferrouillat, *A.* Bois, *E.* Yang, *G.* Lahrech

CentraleSupélec

25 January 2019

Abstract

This report details the sizing of a synchrotron X-Ray beamline enabling coronarian angiography. It aims to present the different parts of the beamline, their functions and the solutions found to implement them. The limitations and opportunities for improvement of those solutions are also exposed.

Contents

Introduction

Angiography is a technique in use in hospitals for control of coronarian arteries. This technique relies on the injection of a contrast agent in the heart of the patient. An image of the patient's heart is made with X-Ray light and the arteries where the contrast agent circulates are therefore visible. Usually the image is realized thanks to traditional X-Ray tube.
The purpose of the medical beamline is to use the synchrotron light source which is up to 10^5 more brilliant than medical X-Ray tubes and enables an improvement of the method. The conditioning of the light beam allows a very specific selection of the desirable wavelengths with a strong brilliance. It also allows to change the chosen wavelengths in order to accommodate various contrast agent. Due to these characteristics of the incident beam, the resolution of the image is very accurate even if the dose of contrast agent injected is less important. The use of synchrotron light therefore allows a less invasive angiography technique.
A synchrotron light is emitted by relativistic electrons subjected to centripetal acceleration. Those electrons are accelerated in a synchrotron ring. An insertion device unleashes the radiation at an inflection of the ring. The light is then channeled in a beamline until it reaches the sample environment. The design of the beamline consists in sizing all of its parts in order to obtain the right light characteristics when the beam irradiates the patient.
The purpose of this report is to present a complete design of the beamline, from the insertion device to the patient and the detectors, in adequacy with all the physical requirements for the angiography to achieve.

Part I
Technical choices and conception

1 General description of the beamline

The purpose of the beamline is to carry the light beam from the point of the storage ring where it is created to the sample being studied. It is therefore composed of different devices, which handle the beam and steadily shape it in order to achieve the angiography.

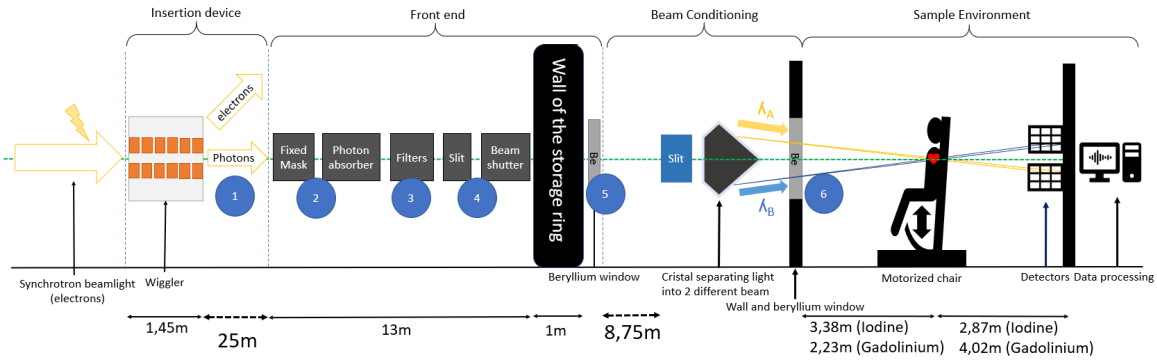

Figure 1: Schematic diagram of the beamline

1 : At the output of the insertion device, the emitted pulses of photons are carried along an ultra-high vacuum conduct, which section is about 20 cm^2. The beam is strongly focused and diverges slowly all along the conduct.
2 : About 25 m from the output of the insertion device is the fixed mask, which is one meter long and absorbs an important part of the beam's energy.
3 : The Front-end is a security device which triggers only in case of air leak in the conduct. It is basically 13m long and does not shift the beam in normal condition.
4 : The filters are a set of thin aluminum and graphite blocks which remove the low part of the light spectrum and absorb an important part of the incoming power. This part of the line is 2.5 m long.
5 : The primary slit is a pinhole of about 3 m long which strongly reduces the beam's energy. It is an adjustable device which permits to set the power of the beam in the last part of the line. The beam follows the ultra-high vacuum conduct until the monochromator.
6 : The monochromator is the most complex and important device of the line. It allows to extract two specific wavelengths from the radiation. The monochromator is into an enclosure under ultra-high vacuum which diameter is about 1 m. The beam goes out through a small X-ray transparent beryllium plate. It then irradiates the patient's heart and the detectors. The room containing the patient and the detectors is about 10 m long.

2 Physical consideration on the beam

2.1 Insertion device

2.1.1 Definition of insertion device and photon flux

An insertion device is an instrument, which consists in a periodic arrangement of magnets, that generates a light beam, called synchrotron radiation (SR), by stimulating the electrons flux. It is placed right after the storage ring and it represents the first step in the light treatment in the beamline. The goal of the insertion device is to generate a light beam characterized by a specific number of photons per seconds and within a specific energy bandwidth. This quantity is called photon flux. The insertion device purpose is to make the electrons oscillating at microwave frequency in order to radiate photons in the XR spectrum.

2.1.2 General features of electrons dynamics in a magnetic field

For a better understanding of the functioning of such device, it is important to focus on the physical principles involved. Consider an electron moving with circular motion in a uniform magnetic field B perpendicular to the plane of motion (Fig. 2). It results from special relativity that the electron will radiate photons in a cone of $1/\gamma$ angle where γ is the Lorentz factor ($\gamma = 1/\sqrt{1-(v/c)^2}$, v being the electron's speed and c the celerity of light).

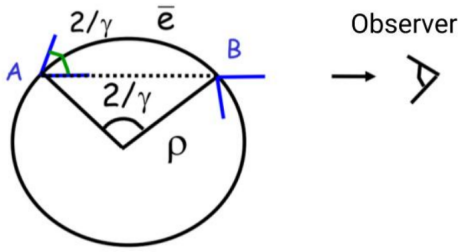

Figure 2: Electron in a uniform magnetic field [12].

If the observer is located on the right side of the circle, he will only observe the radiation emitted by the electron along the $\widehat{AB}$ arc. Hence, the duration of the emission along $\widehat{AB}$ which yields to the pulse duration is given by $\tau = \frac{\rho}{c\gamma^3}$, with ρ the radius of the circle (in m). Then intervenes the concept of critical energy E_c defined by Heisenberg principle $E_c = \frac{\hbar}{\tau}$, where $\hbar = 1.05 \times 10^{-34}$ J$\cdot$s. An equivalent definition is such that it splits the energy spectrum in two parts, as that each part contributes equally to the total power [12].

2.1.3 Bending magnet

A first idea to reproduce the aforementioned phenomenon in the synchrotron setup is to introduce a bending magnet along the storage ring. This element will curve

the electrons' trajectory and thus produce a SR. The spectral angular flux produced F (in photons $\cdot\, \mathrm{s}^{-1} \cdot \mathrm{mrad}^{-1} \cdot 0.1\%$ *bandw*) is given by :

$$F(\lambda) = 2.457 \times 10^{10} \cdot \; I_e \; E_e \frac{E}{E_c} \int_{E(\lambda)/E_c}^{\infty} K_{5/3}(\eta) d\eta \tag{1}$$

where I_e is the electron beam current (in mA), E_e is the energy of the electron beam (in GeV), E_c is the desired critical energy (in the same unit as E) and K_ν is the modified Bessel function of second kind of order ν.

In the figure 3, such function is given for different values of N.

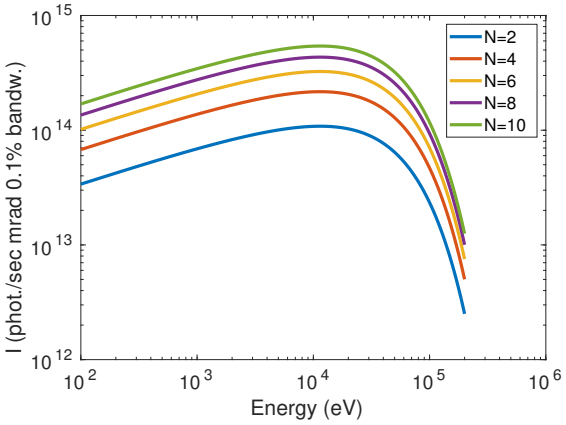

Figure 3: Spectral angular flux plotted with the values in Table 1.

The angular distribution of F can be considered uniform as the deviation [24] is negligible nearly in the whole range of interest, except around the angle $\pm K/\gamma$, so around the borders of the beam 4a.

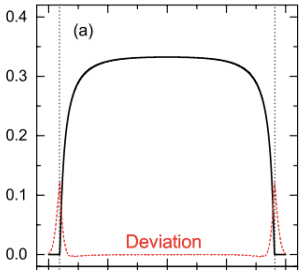

(a) Photon flux (in black) and deviation (in red) for a typical wiggler [24].

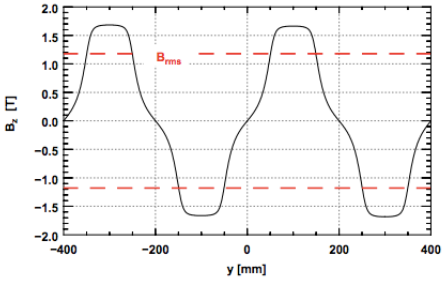

(b) Magnetic field (z component) global trend along direction y[26].

Figure 4: Magnetic field analysis.

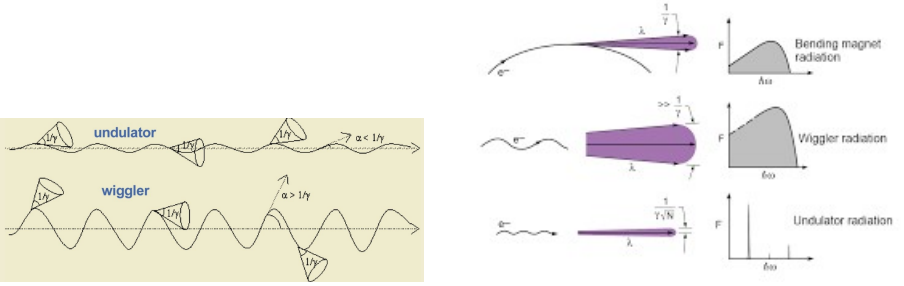

(a) Difference between an undulator and a wiggler. Credits [20]

(b) General shape of the spectrum going out of each insertion device. Credits [3]

Figure 5: Comparison between undulator and wiggler.

2.1.4 Beyond the bending magnet: wigglers and undulators

A bending magnet produces relatively few photons because the electrons are only deviated once. To improve the photon flux, undulators or wigglers are used nowadays. A sinusoidal magnetic field is produced to set the electrons on a sinusoidal trajectory [12]. In practice, the magnetic field (in T) perpendicular to the beam B_z has the typical global trend along the beam direction (y) shown in 4b, but it can be approximated as [12]:

$$B_z(y) = B_0 sin\left(\frac{2\pi y}{\lambda_u}\right) \tag{2}$$

where B_0 is the magnitude of the magnetic field (in T) and λ_u the spacial period of the magnetic field (in m).
Hence, the trajectory of the electrons will be:

$$x(y) = \frac{K}{\gamma}\frac{\lambda_u}{2\pi}\sin\left(\frac{2\pi y}{\lambda_u}\right) \tag{3}$$

where the K factor is defined as:

$$K = \frac{e}{2\pi mc}\lambda_u B_0 \tag{4}$$

where e is the elementary charge (in C), m is the mass of an electron (in kg).
If $K \gg 1$, the device is a wiggler and if $K \approx 1$ it is an undulator.
The electrons are deviated twice a period and they generate a SR at each curve. For this reason the power of the beam is increased. On the contrary to an undulator, the wiggler produces a quasi-continuous spectrum and a large opening (Fig. 5b). As, for the final purpose, the beam shall have a wide opening and a continuous sprectrum, the wiggler results to be the best choice.

2.1.5 Parameters of interest

The wiggler's characteristic parameters must be set in order to obtain the desired flux for the final purpose. To achieve such objective an ensemble of equations has been gathered and solved.

E_e	σ	I_e	P	F^*	$E_1[E_2]$	E_c
6.0 GeV	489.7 μm^2	200.0 mA	18 kW	$\sim 10^{15} phot.s^{-1}$	$E_c - 5[+5]$ eV	40 keV

Table 1: Parameters of the electron beam at ESRF and desired output values for the beamline.

B_0	L	N	λ_u	K	gap
1.68 T	1.41 m	10	14.0 cm	22	18.0 mm

Table 2: Wiggler insertion device parameters

The parameters of the electron beam are set according to the features of the storage ring : the energy of the electrons E_e, the intensity of current I_e and the transverse size of the electron bunch σ. Moreover, coherent values of power P, the critical energy E_c and photon flux F^* within an energy window $[E_1, E_2]$ are set according to the constraints and the final aim of the whole beamline (Table. 1).
From the critical energy and the energy of the electron beam is deduced the amplitude of the magnetic field B_0 (in T) :

$$B_0 = \frac{E_c}{(0.665\ E_e^2)} \tag{5}$$

Moreover, it is possible to determine the length of the wiggler L (in m) and the number of periods of the magnetic field N generated in the device from the power, the electron current and the photon flux through the following expression :

$$L = \frac{2P}{(1265.382\ I_e\ E_e^2\ B_0^2)} \tag{6}$$

$$N = \frac{F^*}{\int_{E_1}^{E_2} F(E)dE} \tag{7}$$

Finally, the period of the magnetic field in the wiggler λ_u (in m) is

$$\lambda_u = \frac{L}{N} \tag{8}$$

The aforementioned parameter K, given by the equation 4, can also be computed. All the obtained parameters which characterize the wiggler insertion device are displayed in the table 2.

2.1.6 Choice of the magnets

The type of magnets used in the realization of the wiggler device represents an important feature: there are superconducting magnets, electromagnets and permanent magnets.

Electromagnets are magnets in which the magnetic field is produced by an electric current. They can produce fields that significantly exceed 2 T and they allow to shape with precision the magnetic field. Superconducting magnets allow the tailoring of a perfect sinusoidal field up to 10 T. Finally, permanent magnets are magnets that retain their magnetic properties in the absence of an inducing field or current. Electromagnets and superconducting magnets require a significant power supply to achieve intense fields, on the contrary of permanent magnets, which therefore result to be the best option in terms of benefit-cost ratio.

2.1.7 Choice of the magnet material

Samarium cobalt and neodymium iron boron (NdFeB) are used nowadays as permanent magnet in wigglers. The latter being more powerful, it is the best choice as it leaves a reasonable gap between the jaws for the vacuum chamber. It can be noted that the chosen magnets are characterized by a critical temperature, given by 230°C, over which the demagnetization occurs. Since such thermal values will not be achieved, it is not necessary to monitor the temperature.

2.1.8 Magnet design: two networks

It is also possible to create a sinusoidal magnetic field with permanent magnet by putting them alternatively in 4 directions as described below (Fig. 6a). The magnetic field created is nearly purely sinusoidal. To improve the field strength, one can opt for a hybrid design that uses steel vanadium permendur in addition to neodymium iron boron (Fig. 6b).

2.1.9 Magnetic forces

Neglecting fringing effects and supposing that the volume of the gap is much smaller than that of the magnetized material, the force (in N) is:

$$F_M = \frac{< B^2 > LW}{2\mu_0} \tag{9}$$

Where W is the transverse size of the magnetized surface (in m), μ_0 is the permeability of space (in $\mathrm{H} \cdot \mathrm{m}^{-1}$) and $< B^2 >= \frac{B_0^2}{2}$ for a sinusoidal field. The total magnetic force was estimated to be $F \approx 140$ kN.

2.1.10 Trajectory correction

Finally, the electrons beam shall be in axis with the wiggler device: a technique which allows to correct the beam trajectory at the exit of the device is therefore adopted. To achieve such aim, by setting the resulting force along the path to be zero, is obtained the so called matching condition, according to which the bending angle of the entire device results equal to zero.

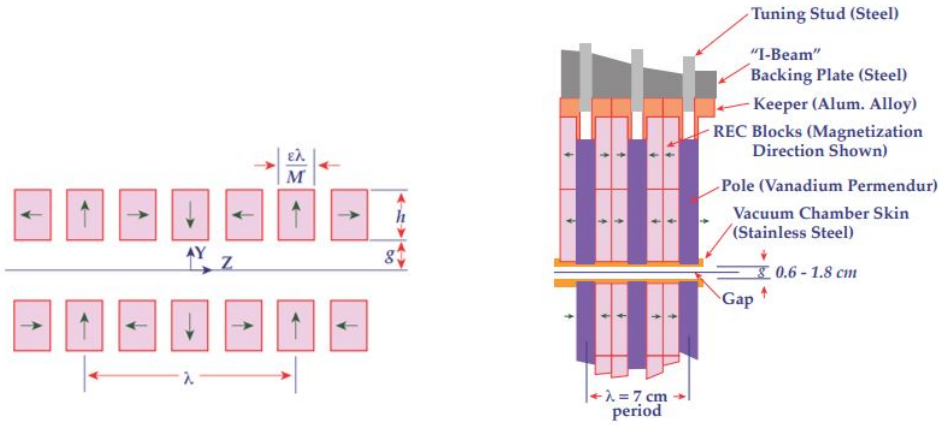

(a) Vertical cross section of a pure rare-earth neodymium iron boor wiggler with four blocks per period. The electron beam moves in the z direction. The arrows indicate the direction of magnetization. [7]

(b) Vertical cross section of a hybrid wiggler using rare-earth neodymium iron boor material plus steel varendium permendur poles. [7]

Figure 6: Comparison conventional and hybrid magnetic arrangement.

$$\int_0^L B_z(s)ds = 0 \tag{10}$$

This condition is often realized by adding a magnet pole of half the length of a normal pole at the entrance and the exit of the magnet, as displayed in figure 7.

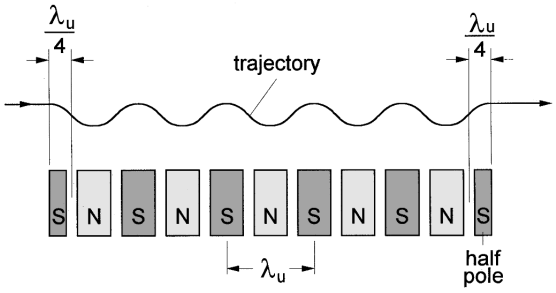

Figure 7: Matching condition for the electrons beam [27]

2.1.11 Determination of the magnets gap

At this point, it is possible to determine the value of the gap between the two arrays of magnets. To obtain such result, the following equation [16], that takes in consideration the use of NdFeB for the permanent magnets, is considered :

$$B_0 = 3.27\ exp\left[-\frac{gap}{\lambda_u}\left(5.08 - 1.54\frac{gap}{\lambda_u}\right)\right] \tag{11}$$

This non-linear equation can be solved by using a root finding algorithm such as *fzero* available on Matlab. The value is given in the table 2.

2.2 Front end

2.2.1 Beam angular divergence and power density

The beam propagates along the z-axis. The divergence can be defined as the angle θ (in rad) of increase b (in m) in the beam diameter (x, y) with the distance l (in m) of propagation in z. Since a synchrotron beam is highly collimated, which means that its angular divergence is very small ($\theta \ll 1$), the approximation $\tan\theta \approx \theta$ is valid. Therefore, the beam angular divergence can be expressed as :

$$\theta \approx \frac{b}{l} \tag{12}$$

Since the angular divergence is determined by the insertion device – being different values of angle given to horizontal and vertical orientations (x, y) (table 3) –, the size of the beam after its emission can then be estimated.

θ_y [mrad]	0.2
θ_x [mrad]	4.0

Table 3: Angular divergence of the photon beam.

Furthermore, considering that the beginning of the front-end is located 25 m downstream the middle of the insertion device, using equation 12 , the beam arrives at the front-end with a size of 100 mm × 5 mm.
The existence of this divergence implies that mechanisms to control the size of the beam must be inserted into the beamline in order to add spatial limitation to the photons' free propagation – these devices are generically named "pinholes". This means that unnecessary heat load is also eliminated during this process allowing the experimental section to receive the beam with the required amount of energy and size. In this case, the beam was required to arrive at the beam conditioning section (located 1m after the end of the front-end section) with a size of 30 mm × 5 mm.
To do this, the beam was shaped twice, as shown in the figure 8, where (1) limits the beam size to 35 mm in both directions (x, y) and (2), installed 5.6 m further, limits it to 14 mm × 4 mm.

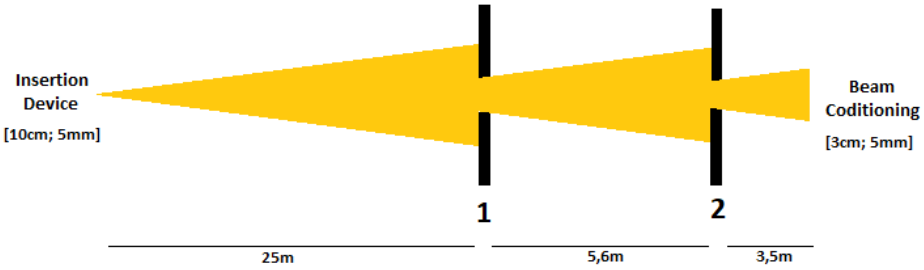

Figure 8: Defining the beam size with pinholes.

This configuration allows the power and the photon flux to be reduced by a factor of approximately 15. This value is obtained from the consideration of the photons' power density, which is not homogeneous (figure 9).

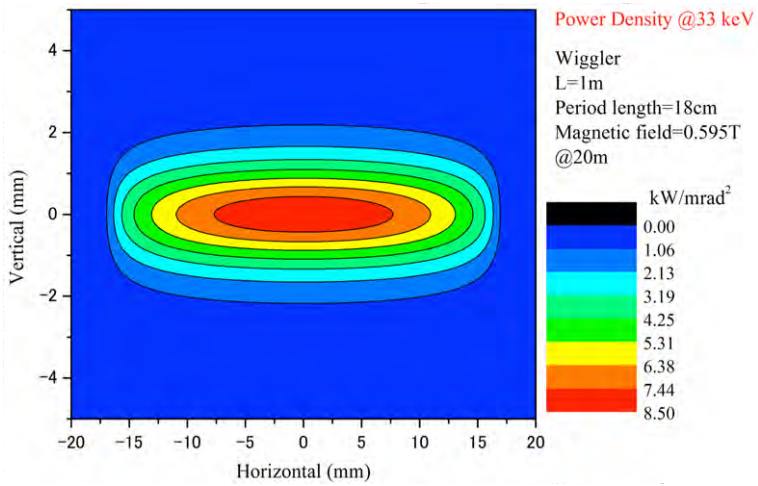

Figure 9: Power density of a photon beam 20 m away from the source. This spectrum was obtained with the software SPECTRA at the SPring-8 Synchrotron.

To initially estimate the power absorbed at the first pinhole[1], an approximation of this spectrum (figure 9) to the spectrum expected for the beam was made assuming that the beam power is almost completely concentrated at the center of the beam. Be in this case a region of 87.5 mm × 2 mm. At the second pinhole[2] the power reduction factor was then estimated as directly proportional to the reduction of the area of the beam[3].

[1]It is the fixed mask described in section 3.2.

[2]It is the XY-slit described in section 3.2.

[3]The power density approximation is explained with more details in Appendix D - Front-End Appendix

2.2.2 Filters

Filters are used to lower the number of low energy radiations which are irrelevant for the angiography; namely, energies lower than 35 keV for iodine-contrast angiographies and 50 keV for gadolinium-contrast ones. They absorb a significant amount of the power of the beam in order to transmit only what is needed downstream. More precisely, filters are designed to send the exact amount of photon flux in the spectrum range selected by the monochromator.

The log-log graph below shows the whole effect of the Front-End on the photons flux, it takes into account the absorption from both splits and filters. The front-end reduces significantly the photon flow, especially for low-energy radiations. As the photons energy range selected by the monochromator is way thinner for a Iodine angiography than for a Gadolinium one, the Front-End needs to absorb much power when Gadolinium contrast agent is used. This differentiation requires to change the thickness of the filters used. Figure 42 details the different layers of graphite and aluminum used for each contrast agent.

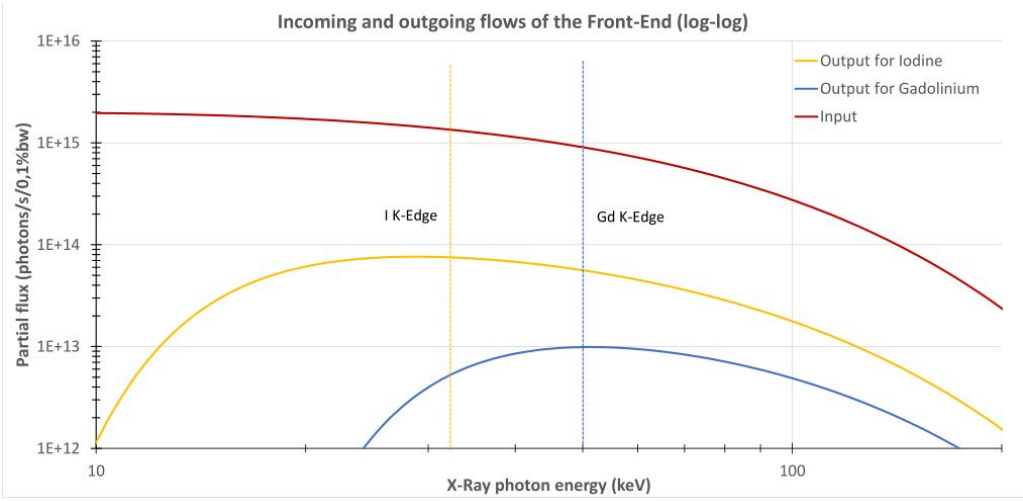

Figure 10: Incoming and outgoing flows of the Front-End

Concretely, filters are thin foils and blocks of materials on the beam trajectory which transmit a given proportion of incoming photons. This proportion, called transmittance, increases with the energy of incoming photons. This explains why filters reduce the low energy radiations. Transmittance also decreases with the density and the atomic number of the absorber and, of course, increases with the thickness of the foil. Therefore, materials and dimensions of the filters are chosen to fit the needed transmittance.

As far as materials are concerned, graphite is the preferred material for filters, because of its low price and high fusion temperature. But aluminum is also a

good complement because of its higher atomic number and good cooling properties. Lastly, thin beryllium windows are often put downstream of the filters to prevent molecules from going upstream without altering the beam. Indeed, as low energy radiations have already been absorbed by the filters and the atomic number of the beryllium is low, these windows absorb almost nothing.

2.3 Beam conditioning

In order to properly scan the heart of the patient in three dimensions, two monochromatic beam lights with specific wavelengths are required. It is therefore necessary to condition the white beam after the front end. This operation is conducted in a monochromator, which contains a silicon crystal and relies on Bragg and Laue laws on diffraction (described in appendix A).

2.3.1 Optical geometry of the monochromator

Physical concept of the monochromator As previously mentioned, two monochromatic beams with specific wavelengths must be extracted from a poly-chromatic beam. The energy, and therefore the wavelengths of the photons are set by the imaging requirements : $E_1 = 33.30\,\text{keV}$ and $E_2 = 32.70\,\text{keV}$. The solution designed needs to be easily implementable and to fit the requirements.
In order to have two specific wavelengths, at least two different angles of incidence between the incoming beam and the Bragg plans are needed to fit the requirements [13]. Thus, the solution is a unique, curved Laue crystal made of a wafer of silicon, (100) oriented following Miller's notation, as shown in the figure 12. The crystalline planes are perpendicular to the surface, and the angle of incidence varies along the wafer. A pair of slits placed above the wafer selects two beams, that are after diffracted by the wafer of silicon. The angles at stake in the crystal are of the order of 10^{-2} rad. The curvature can be adapted to the wavelengths required by the contrast agent.

Principle of the filter : two slits In order to select the two wavelengths, a copper cone pierced with two slits is placed upstream of the crystal. The tip of the cones might be designed in a different material in order to be sharpened in a more precise way. To allow the slits to be adaptive to the contrast agent, the cone is made of two parts bonded one with the other. In each part, the gap between the two slits is different to intercept the beam at different Bragg's angles, as seen in figure11.

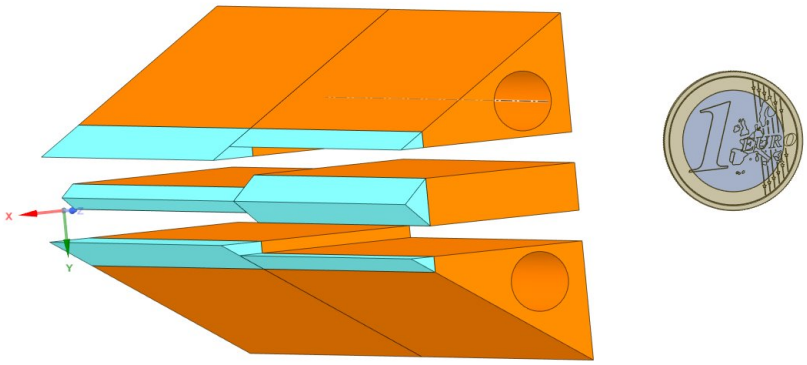

Figure 11: Schematics of the slits designed on SpaceClaim (on scale with the coin, except the width of the slits)

A simple piston allows to shift the cone from one position to the other. The two slits are 10 µm wide and let only two horizontal thin beams pass through and reach the crystal with two different angles. The width of these slits is narrow enough to select a precise range of wavelengths, but it also takes into account the feasibility of such slits. Indeed 10 µm slits are common in synchrotrons. Diffraction due to the size of the slits is neglected, because of the wavelength at stake. Indeed, the typical diffraction angle given by $\theta = \frac{\lambda}{e}$ with e the width of the slit, gives $\theta \approx 10^{-5}$, which can be neglected compare to the natural divergence of the beam.
The precision on $\frac{\Delta\lambda}{\lambda}$ for the two different contrast agents is different :

$$\left(\frac{\Delta\lambda}{\lambda}\right)_{Iodine} = 1.61 \cdot 10^{-5} \tag{13}$$

$$\left(\frac{\Delta\lambda}{\lambda}\right)_{Gadolinium} = 7.45 \cdot 10^{-5} \tag{14}$$

This comes from the relation (15) coming from a proportionality relationship on the flux intercepted by the crystal :

$$\Delta\lambda = |\lambda_2 - \lambda_1|\frac{d}{e} \tag{15}$$

Where λ_1 and λ_2 are the two wavelengths requested by the sample environment, d is the width of the slits and e the vertical width of the beam.

Constraints and attenuation of the beam Through the monochromator, the beam loses a part of its power, first because only two thin bands pass and second because the filter absorbs a certain amount of energy.
Most of the photons with the same energy finish on the copper between the two slits. The division of power is thus made with a factor $\frac{d}{e}$ where d is the width of the

slit and e the vertical size of the beam :

$$\frac{\Phi_{slits}}{\Phi_{incident}} = 5 \times 10^{-3} \tag{16}$$

Although this does not represent a big loss in comparison, an amount of power is also absorbed by the thin crystal. The absorption is simply given [9] by the Beer-Lambert law (17), where μ_r is the inverse of the characteristic distance of attenuation for such wavelengths in silicon (in μm^{-1}), h is the thickness of the crystal (in μm)and $\sin\theta \approx 1$ as seen in the figure 12.

$$\Phi_{out} = \Phi_{in} \exp\left(\frac{-\mu_r h}{\sin\theta}\right) \tag{17}$$

The absorption depends on the wavelengths concerned, and to give a a common value for each contrast agent :

$$\left(\frac{\Phi_{absorbed}}{\Phi_{slits}}\right)_{iodine} = 1.6 \times 10^{-2} \tag{18}$$

$$\left(\frac{\Phi_{absorbed}}{\Phi_{slits}}\right)_{Gadolinium} = 5 \times 10^{-3} \tag{19}$$

Given this figures, the reduction factor of the whole monochromator is then given by :

$$\left(\frac{\Phi_{out}}{\Phi_{in}}\right)_{iodine} = 1.157 \times 10^{-3} \tag{20}$$

$$\left(\frac{\Phi_{out}}{\Phi_{in}}\right)_{Gadolinium} = 1.172 \times 10^{-3} \tag{21}$$

2.3.2 Dimensioning of the wafer

The method followed is thus a backwards induction reasoning. For a particular contrast agent, the monochromator must output two beams with photons of energy E_1 and E_2 mentioned above.
The angles of incidence on the crystal planes θ_1 and θ_2 are defined by Bragg's law :

$$(\lambda_1; \lambda_2) = \left(\frac{h \cdot c}{E_1}, \frac{h \cdot c}{E_2}\right) \tag{22}$$

$$(\theta_1; \theta_2) = \left(\sin^{-1}\left(\frac{\lambda_1}{2d_{100}}\right), \sin^{-1}\left(\frac{\lambda_2}{2d_{100}}\right)\right) \tag{23}$$

In figure (12), angular geometry allows for i = 1 or 2 :

$$\alpha = \theta_1 - \theta_2 \tag{24}$$

Assuming for the computation:

$$C = \frac{e}{l} \tag{25}$$

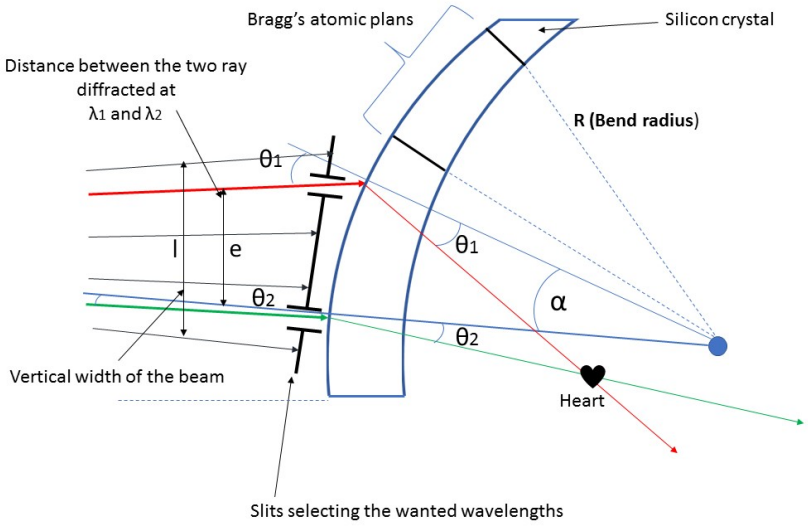

Figure 12: Bent monochromator system

l is easily calculated in the figure 12, thanks to the original width of the beam just outside the pinhole and the beam's dispersion (parameters given by the Front-End team). Furthermore, the distance between the ray diffracted at λ_1 and λ_2 noted e is chosen as compared to l with the choice at C. This parameter allows to play on the bend radius, with :

$$C \leq 1 \tag{26}$$

The radius bend will be way higher (of the order of 10 meter) than the incidence distance (of the order of a centimeter). As a consequence, the the radius of curvature (R) is very high compared to the beam's incidence width (e) :

$$\alpha = \frac{e}{R} \tag{27}$$

The radius of curvature of the crystal R is determined by the difference of Bragg's equations (18).

$$R|\lambda_1 - \lambda_2| = 2d_{001}e\cos\left(\frac{|\theta 1 + \theta 2|}{2}\right) \tag{28}$$

It is important to note that the radius bend is not identical for iodine and gadolinium because the expressions of θ_1 and θ_2 and therefore the expressions of λ_1 and λ_2 intervene in the formula above.

Finally,

$$\left\{ \begin{array}{l} C_{iodine} = 0.5 \text{ m} \\ R_{iodine} = 6.74 \text{ m} \\ \alpha_{iodine} = 6,31 \times 10^{-4} \text{ rad} \\ \theta_{\lambda 1,iodine} = 3.44 \times 10^{-2} \text{ rad} \\ \theta_{\lambda 2,iodine} = 3.50 \times 10^{-2} \text{ rad} \end{array} \right\}$$

and

$$\left\{ \begin{array}{l} C_{gadolinium} = 0.95 \text{ m} \\ R_{gadolinium} = 4.45 \text{ m} \\ \alpha_{gadolinium} = 1.82 \times 10^{-3} \text{ rad} \\ \theta_{\lambda 1,gadolinium} = 2.19 \times 10^{-2} \text{ rad} \\ \theta_{\lambda 2,gadolinium} = 2.37 \times 10^{-2} \text{ rad} \end{array} \right\}$$

2.3.3 Measures's tolerances

Thanks to equation 18, the incertitude on the bend radius R can be estimated :

$$\frac{\Delta R}{R} = \frac{2\Delta\lambda}{|\lambda_1 - \lambda_2|} + \tan\theta\Delta\theta \tag{29}$$

Knowing that the incertitude on $\frac{\Delta\lambda}{\lambda}$ has to be at most 10^{-4}, the incertitude tolerance on R can be deduced from:

$$\frac{\Delta R}{R} \leq \frac{2\lambda}{|\lambda_1 - \lambda_2|} \times \frac{\Delta\lambda}{\lambda} \leq 10^{-2} \tag{30}$$

Then for iodine,

$$R_{iodine} = 6,74 \pm 0,07 \text{ m} \tag{31}$$

And for gadolinium,

$$R_{gadolinium} = 4,45 \pm 0,05 \text{ m} \tag{32}$$

2.4 Sample environment

2.4.1 Contrast agents, K-edge and wavelengths

As mentioned above, the principle of an angiography is based on X-ray imagery techniques and on the injection of radio-opaque contrast agent into blood vessel. In this case, the agent is either iodine or gadolinium. K-edge is the energy limit over which higher energy photons will be absorbed. Contrast agents with high K-edges are used because they make it possible to work with high energy beams. Once the contrast agent is chosen, the energy of the beam - and therefore its wavelength - must be determined. Here, differential imagery will be performed to get an image of the patient's heart and vessels. In order to do that, two beams with different energies will be needed : one, named A, above the K-edge, and another, named B,

under it.
By using those two wavelengths, two images will be detected and substracted one from another, which gives one final exploitable image.

2.4.2 Characteristics of the light

In order to get a good image quality, the patient's heart must be scanned with both wavelengths at the same space and time. Therefore, the synchrotron beam was designed so that it will send a beam that is the sum of two monochromatic beamlight, each having λ_A and λ_B as wavelength. The beam will be separated into two different beams as shown in 12 that will intersect at the heart of the patient as shown in the schema.

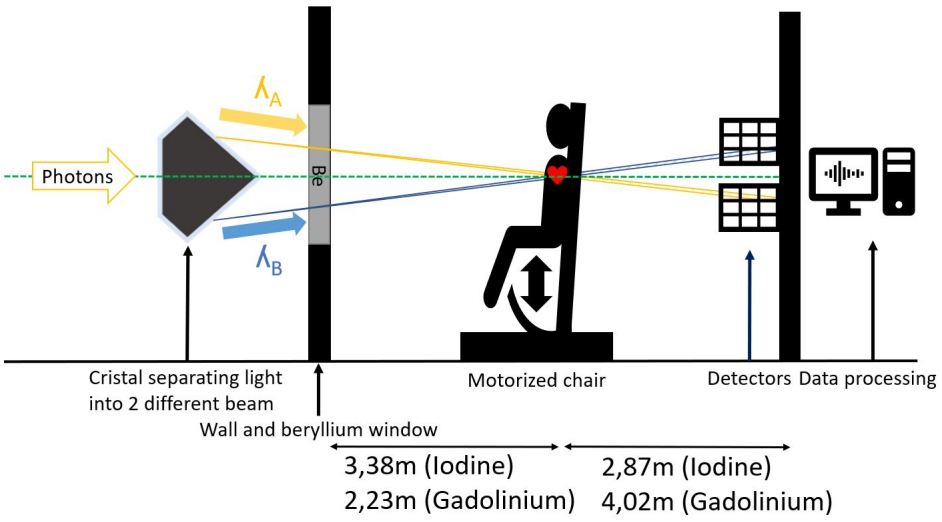

Figure 13: Schema of the angiography process

Thanks to the crossing beams, the heart can be scanned without delivering the entire amount of power the synchrotron could deliver. That way, the patient will receive less radiations and less health deterioration.
Afterwards, the remaining light will be collected by two rows of detectors, each one collecting photons at a determined wavelength. The logarithmic substraction allows for increasing the contrast at the level of the heart.

2.4.3 Description of the detector

The detector is composed of two rows of 432 pixels each. Each pixel is 300 µm wide and 10 mm high and the distance between two pixels is 50 µm. This gives a width of 15.1 cm for the image. Likewise, the beam will have approximately the same width. As the chair moves vertically, 432 photon packets will be sent to the detectors to

get a square image with 432×432 square pixels of side 350 µm.
In order to get an acceptable image quality, the "Signal to Noise ratio", defined by :

$$SNR = \left(\frac{\Delta\mu}{\rho}\right)_j c_j \sqrt{\frac{N}{2}} \tag{33}$$

is computed where $\left(\frac{\Delta\mu}{\rho}\right)_j$ is the difference of the mass absorption coefficient values, respectively, above and below the edge, c_j is the mass-density [kg.m^{-2}] of the agent in the artery, and N is the number of photons collected in a given pixel of the detector. *SNR* must remain equal or greater than 5, which therefore gives a minimal value of the number of photons required.
The values of the mass absorption coefficient for iodine and gadolinium were found in [10] and using [14]. The acceptable mass-densities of iodine and gadolinium were computed using data from [5], [4] and [10].

Nevertheless, the heartbeat will induce deformations of the image which will have to be corrected by an image processing.

2.4.4 Health of the patient

The exposition to X-rays can obviously be dangerous if the exposure time is too long, of if it carries too much energy. The associated tool to measure the absorbed dose of X-rays is D, in Gray, defined by :

$$D = \Delta t \sum_i E_i \left(\frac{\mu}{\rho}\right)_i \phi_i \tag{34}$$

where Δt (s) is the exposure time, E_i (J) the energy of the beam, ϕ_i (s^{-1}.m^{-2}) the number of photons it carries and $\left(\frac{\mu}{\rho}\right)_i$ (m^2.kg^{-1}) is the mass absorption coefficient of the object considered.

Hence, it results in a maximal value of the photon flux in order not to irradiate the examined patient.

2.4.5 Physical constraints

As seen above, (33) and (34) define constraints that must be respected in order to get a sufficient image quality while keeping the patient safe. Those constraints depend on the wavelengths (i.e. on the energies) of the photons because the mass-density c_j, the mass absorption coefficients $(\mu/\rho)_j$ and, of course, the energy E_j depends on it. Therefore, an appropriate choice of wavelengths is crucial, and it cannot be made independently of the other parts of the line.

In the case of iodine, the total number of photons arriving on the detector should stay over $9,6 \times 10^9$ and the number of photons getting to the patient under $4,05 \times 10^{11}$. For gadolinium, the extreme values are respectively $8,64 \times 10^{10}$ and $5,16 \times 10^{11}$.

2.4.6 Absorption

From its creation to the exit of the monochromator, the beam travels in vacuum, whereas between the monochromator and the detector it goes through air and through the patient, that absorb a certain proportion of the light, which strongly depends on the wavelength (because the energy decreases exponentially with the absorption coefficient and with the distance travelled).
Knowing the proportion of photons absorbed between the monochromator and the detector or to the patient makes it possible to compute the minimal and maximal number of photons required at the end of the monochromator for each wavelength in order to satisfy the constraints.

Contrast agent	Iodine		Gadolinium	
K-edge (in keV)	33,17		50,2	
Beamlight	A	B	A	B
Energy (in keV)	33,3	32,7	52,2	48,2
Wavelength (in pm)	36,9	23,8	38,1	25,8
Proportion on the patient (%)	97	97	98	98
Proportion on the detector (%)	4,3	3,6	3,8	3,3
Min. number of photons needed ($\times 10^{11}$)	1,11	1,25	1,20	1,33
Max. number of photons needed ($\times 10^{11}$)	2,09	2,09	2,63	2,63

Table 4: Absorption and requirements at the end of the monochromator for different beams and different contrast agent

As Table 4 shows, the body of the patient absorbs way more light than the air, which is due to the fact that water (that composes most of the body) is about 1000 times denser than the air.

The mass absorption coefficient values for the air and the water were found in [8] and [23].

3 Dimensioning of the solutions

3.1 Insertion device

3.1.1 Vacuum chamber

Concerning the vacuum chamber, the structure adopted is an extruded aluminium narrow profile, characterized by an elliptical cross-section of 22.5 mm × 15 mm. Such profile has been chosen as proposed for the ESRF [2]. The dimensions of the vacuum chamber are coherent with the gap dimensions obtained (Table: 2), as the gap actually results to be thicker.

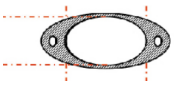

Figure 14: Transverse section of the vacuum chamber [2]

3.1.2 Magnetic and supporting structures

According to our expert, were determined the effective dimensions of each magnet. These are given in the table 5. The magnets are being held into the aluminum keeper by bolts made from non-magnetic material, as illustrated in Fig. 15. The aluminum keeper is then mounted to the backing beam, again using non-magnetic bolts and the whole system is supported by the two girders. The materials that have been used in the study along with some of their features are listed in table 6.

Length	Width	Height
$\lambda_u/3$	10× gap	$\lambda_u/3$

Table 5: Size of the magnet.

3.1.3 Backing beam analysis

A force analysis was performed in order to dimension the backing beam. The forces that dominate the system are the combined weight of the magnets, the backing beam and the aluminum keeper, noted W, the magnetic force F_M and the forces

Material	SAE 316L	A6061-T6
Young Modulus	200 GPa	68.9 GPa
Relative magnetic permeability	≤ 1.03	1.00
Density	8.03 g/cm^3	2.70 g/cm^3

Table 6: Materials features.

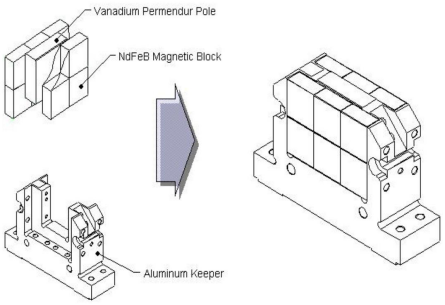

Figure 15: Aluminium keeper. [15]

Material	Length	Width	Height	Weight
SAE 316L	1410 mm	$260mm$	$350mm$	$\sim 1t$

Table 7: Backing beam dimensions.

due to the two supports F_A and F_B, whose distance was to be optimized. An estimation of the total weight indicated that its value is of an order of magnitude of N, whereas the total magnetic force was found to be of an order of magnitude of kN. Therefore, as the weight represents ~1-2% of the forces applied on the beam, and thus its contribution is negligible. Moreover, as there are no forces in the transverse dimension, the problem can be considered two-dimensional. The two supports are assumed to be rollers and thus the beam is isostatic. The magnetic load was derived using the equation Eq 9 and its value was found to be around 100 kN/m. The load is uniformly distributed on the beam. Concerning the constraints, the support points for the backing beam were located to achieve minimum deflection of $30mu$m. Therefore, the optimal distance was found to be 0.24 times the length of the beam. The design characteristics of the beam are presented in the table .

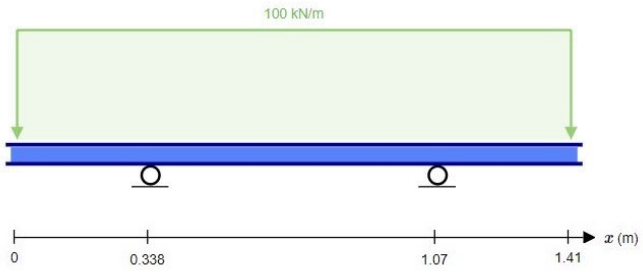

Figure 16: Schematics of the charged beam.

3.1.4 Wiggler assembly

The general structure of the wiggler is presented in Fig. 17 and it is built around the vacuum chamber. The full assembly of the wiggler consists of 2 backing beams

(whose measures are described in Fig. 18), each of one of which is constituted of 21 supporting magnet support, 22 neodymium magnets and 21 vanadium permendur poles (whose dimensions are described in Fig. 19).

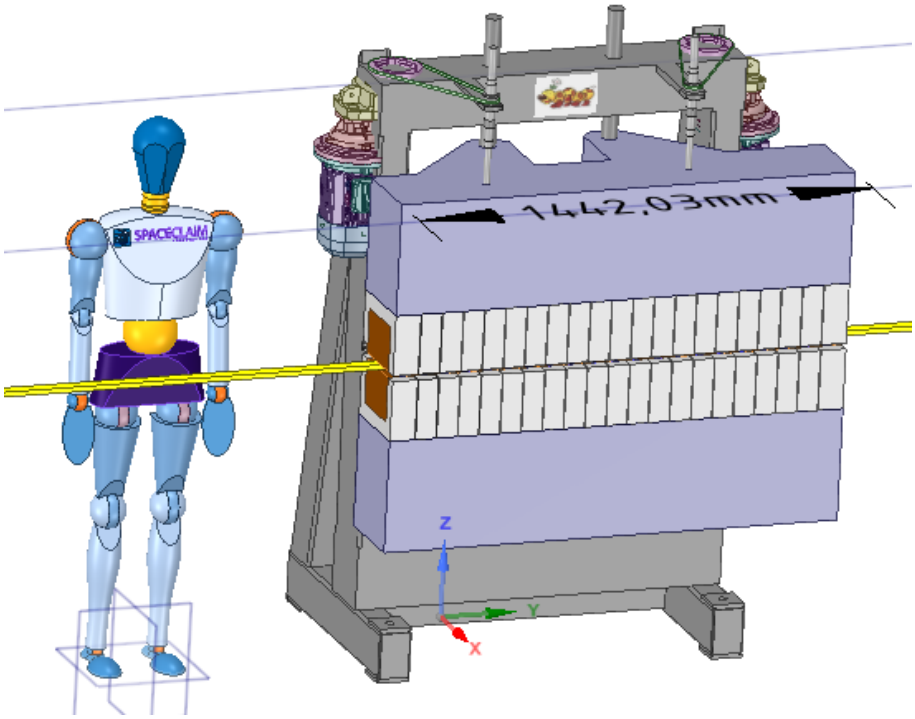

Figure 17: General overview of the wiggler.

3.1.5 Drive and control system

It is fundamental to check that the two jaws of the wiggler are perfectly symmetrical with respect to the electron flux and that the gap between them is kept constant. To control the position of the jaws, precision rolled ball screw from SKF® (described in Fig.21a and Fig.21b) are adopted. The driving function and the translation function are separated: the screw is responsible for the translation and the guides strips undertake all the moments in order to guide both the jaws according the same translation axis 20.
This allows to transform the rotational effort of the motor in the translation of the jaws with a very high yield, up to 90%/95%. Moreover, this actuator technology has better precision and mechanical response to vibrations when compared to the hydraulic one. The model that could be used in this case is called PND DIN69051 and has a diameter of 63mm, a thread of 10mm and a precision G5. The moment that must be imposed at the nut in order to have a movement of the magnets, considering the force imposed by the magnet, is given by Eq.35.

$$T = \frac{FP_h}{2000\pi} \tag{35}$$

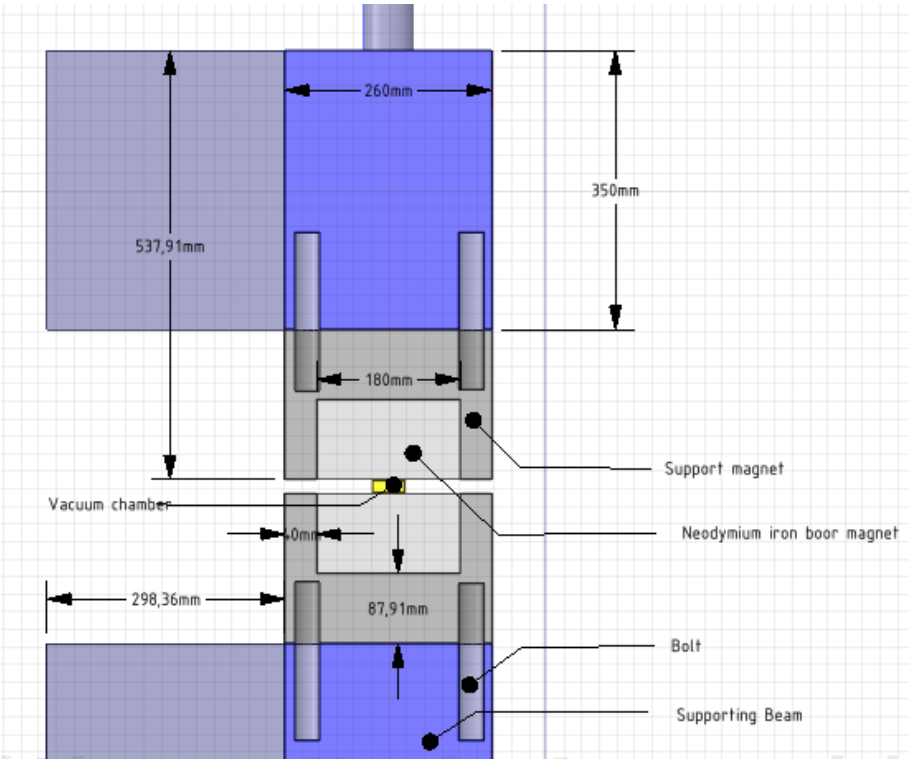

Figure 18: Side view of the wiggler.

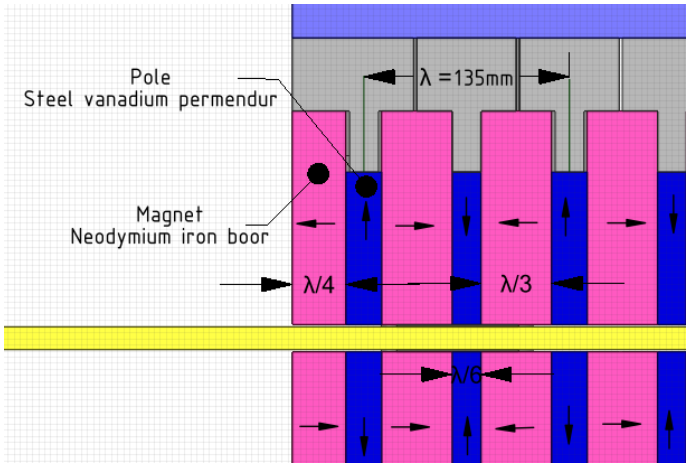

Figure 19: Magnet network.

Where T is the moment (in $\mathrm{N} \cdot \mathrm{m}$), F is the force imposed in the axis of the screw (in N), P_h is the thread of the screw (in mm).

The precision of the screw nut system[4] from SKF® fits the µm precision. The class F gear motors (Fig.23) from Bonfiglioli® can deliver moments from 140Nm to 14000Nm to match the magnetic load moment (~1kN). In order to control the four

[4] https://www.skf.com/binary/81-149715/Precision-rolled-ball-screws—6971_1-FR.pdf

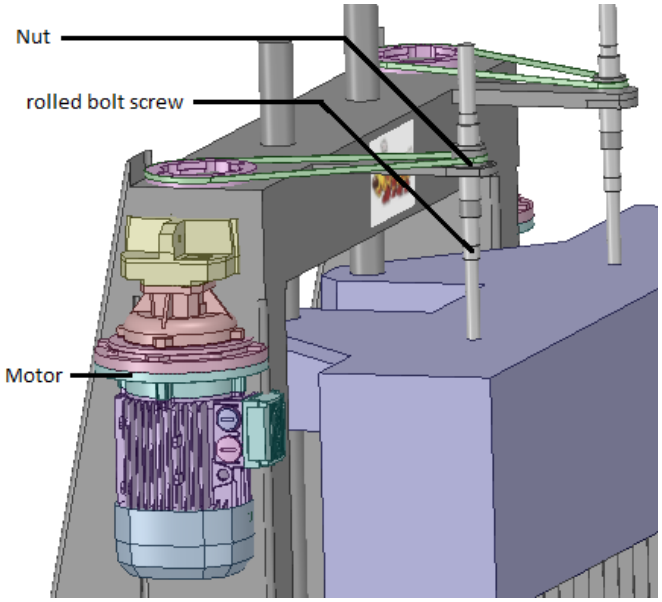

Figure 20: Guiding part.

motors, the motion control and the interface[5] of Bonfiglioli® are installed on the system (Fig.22b). A safety brake is added to the motor in case of dysfunctioning. The brake is maintained open but when the safety button is pushed, the brake is released and stops the motor from rotating. In order to be able to lift the jaws higher for maintenance or to adjust the gap manually, a crank is added to the motor axis. The radius of crank is set to be 50cm which enables a human to control the gap manually thanks to the high reduction ratio of the gear motor.

3.1.6 Sensors

To be able to measure precisely the gap between the jaws and make sure the theoretical parameters are set, an optical fibre sensor is placed on both jaws: optoCONTROL CLS-K of the company micro-epsilon®. When the distance goes below the security nominal value located just above the vacuum height chamber, the sensor sends a signal to motor and the emergency brake is released.

[5]https://www.docsbonfiglioli.com/pdf_documents/catalogue/VE_CAT_BMI_STD_ENG_R01_2.pdf

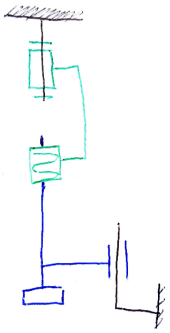

(a) Cinematic schematic the support. In green, the stepper motor and the rolled balled screw. In blue, the beam loaded with the magnets. In black, the guiding bars. Not at scale.

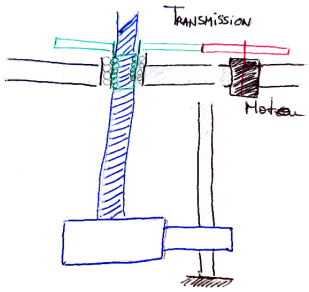

(b) Sketch of the support. Not at scale.

Figure 21: Guiding part of the Wiggler.

(a) Bonfiglioli® class F motor

(b) Bonfiglioli® interface solution

Figure 22: Guiding part of the Wiggler.

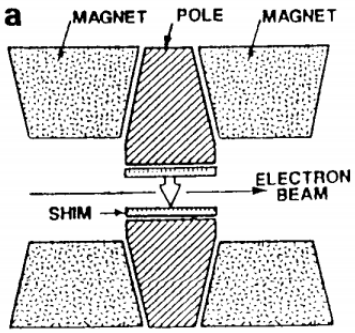

Figure 23: Iron shims placed on the poles of a wedged hybrid wiggler. Credits [11]

3.2 Front end

The design of the front-end needs to take into account a set of components with different roles. These roles can be grouped as: (1) protection of the ultra high vacuum of the synchrotron ring, (2) shielding of radiation to human safety, (3) first shaping of the photon beam (in size and energy), and (4) monitoring of the beam positioning [6].
In this sense, considering the constraints of this work, the general Front End layout is described in figure 24, where the main role of the components is informed. The Front End begins at the storage ring and ends downstream the shield wall.

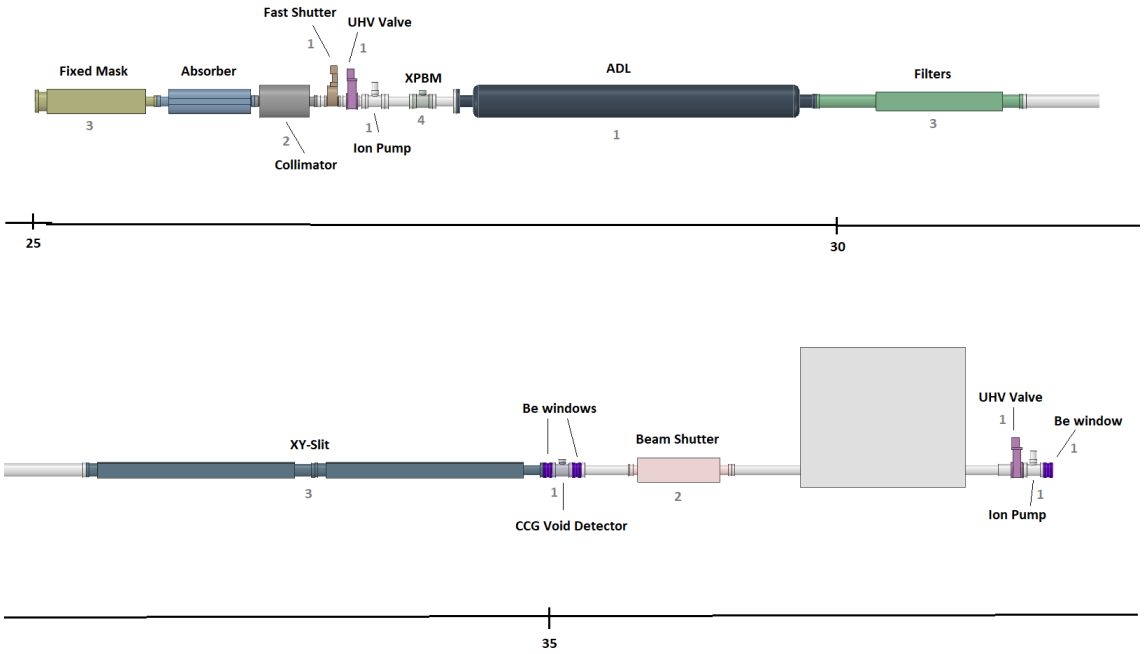

Figure 24: Front-end layout, informing components used for (1) ultra high vacuum protection, (2) radiation shielding, (3) beam shaping and (4) beam positioning monitoring.

Ion pumps, UHV valves and a beryllium window are used to protect the ultra high vacuum of the storage ring. A fast shutter, Acoustic Delay Line and a Cold Cathod Gauge (CCG) vacuum detector are used to rapidly isolate the beamline in case of a leak in the system. For human safety, there are a beam shutter made of W and a collimator made of Pb. All the components of the front-end (excepted a UHV valve and the Beryllium window) are installed inside the synchrotron beam ring, as another measure of human protection. Pb blocks for shielding the most scattered off-axis x-ray are also placed around the pipe before its penetration through the wall.

Besides, to shape the beam size according to what was described in the section 1.2.2, it was installed in the front-end a fixed mask – to define the beam size accepted at the beamline –, filters – to absorb low energy photons – and a XY-slit – to define the beam size required by the beamline users. These three components also handle the high heat load of the system, reducing the power density. When the beamline is closed, it is up to the photon absorber to completely intercept the power that is not absorbed by the mask [21].
Finally, the XBPM (X-ray Beam Position Monitor) monitors if the beam is positioned accurately.
Detailed informations about the components of the Front End are described below.

3.2.1 Keeping the beamline safe

Shutting off the beam In case of emergency, or simply for maintenance, the beam has to be killed and the operators must be protected from the heat and occasional radiations.
This is done through a combination of three components. The first one is a fast shutter, that activates in case of a leak of air that would happen downstream in order to protect the rest of the synchrotron. This fast shutter needs to close in a few milliseconds and must be able to withstand the full beam for this duration. The second one is the photon absorber, which is used when one needs to shut off the beam over the duration of the emergency or maintenance. This component is composed of two path that the beam can take. One lets it pass to the rest of the beamline and the other has no exit. The photon absorber is moved vertically to make the beam take one path or the other thanks to a pneumatic mechanism.
This system takes about 1.5s to shut off the beam. A mechanism of the same kind is used to close the beam shutter. This component is used to filter the possible radiations that could escape the photon absorber. It is made of a heavy metal (more than 95% of tungsten).

Choice of a fast shutter The fast shutter used is the same as the one used at SPring-8[1]. Its advantage is its very short closing speed (it closes in less than 10 ms). Its body material is 316L stainless steel (AISI 316L).
The hypotheses and the results presented in the appendix show that this fast shutter is well adapted. With AISI 316L, sustaining the whole beam leads to an increase of about 1200 K and that stays under the melting point of the metal. The fast shutter will then be able to receive the heat of the beam without burning for at least 10 seconds. This leaves ample time for the photon absorber and the beam shutter to rise and take its place.

Acoustic Delay Line In case of a leak happening downstream (for example, due to an error in the maintenance), the incoming particles need to be slowed down to let the time for the fast shutter to close down before the can go upstream into the

electron beam and severely damage the whole installation by being burnt. This is done thanks to the Acoustic Delay Line (ADL) which consists of several little tanks linked only by very small apertures (large enough to let the beam go through when everything goes correctly). Using two articles detailing the speed of such a stream of molecules ([22], [19]), the ADL was designed to be 2 meters long so that particles take about 200 ms to pass through it. This also gives ample time for the fast shutter to close and thus the system possesses a comfortable margin.

Ultra High Vacuum Valve and CCG Vacuum Detector In order to stop the incoming particles, an *Ultra High Vacuum* (UHV) valve coupled with an Ion Pump are set at two points of the beamline. This allows to maintain a UHV in the different parts of the front end, so that it can be isolated when there is a need of a maintenance. To detect if molecules entered the vacuum, a CCG vacuum detector is set between two windows of beryllium, as advised by Prof. Takahashi.

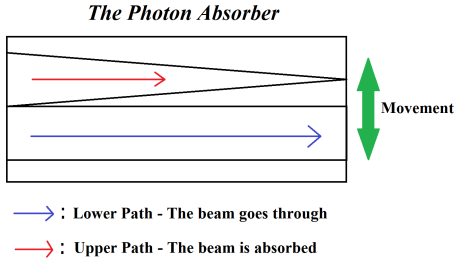

Figure 25: The Photon Absorber

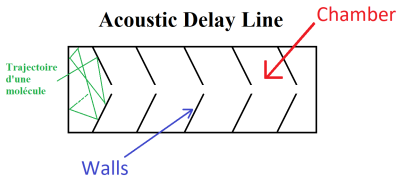

Figure 26: The ADL

3.2.2 Defining the photon beam size: pinholes

Pinholes are the components used to add spatial limitation to the beam size, allowing to pass only the suitable size of the beam. The front-end must provide to the next section a beam with the size of 30mm × 5mm. However, according to equation 12, the photon beam arrives at the front-end section with a size of 100mm × 5mm and the inner diameter of the valves (measuring 40mm) is also a constraint, so that the beam must be shaped right at the entrance of the front-end layout.
To assure this, a mask is placed as the first component in the layout. In this case, the downstream aperture of the mask is designed to measure 35mm, thus defining the beam size to 35mm × 5mm and reducing the power allowed at the beamline by a factor of 2.5. If the beamline is open, the beam is allowed to pass through the collimator, which can absorb the most scattered photons but does not change the beam size.
Placed 5.4m downstream the line, a XY-slit is installed to define the final aperture to shape the beam size as required by the users [21]. In this case, the beam arrives at the slit measuring 57mm × 6mm. As the first component of the beam conditioning section is estimated to be placed 1m after the end of the front-end section, its

pinhole is an aperture of 14mm × 4mm and its power reduction factor is 5.8.
Since these components shape the beam, their designs must consider too the power absorbed during the process.

3.2.3 Design of the elements

As explained in the appendix, the chosen materials and the shapes of the elements are designed to optimize their resistance to the high power of the synchrotron beam. The materials have a high thermal conductivity to be easily cooled down. The pinhole and the absorber are also have a shape that minimize the beam's surfacic power.

3.2.4 Coolant system for the upstream parts

A coolant system based on turbulent water flows is used to remove the absorbed energy from the different components: the fixed mask, the filters and the slit. All of the details and calculations can be found in the appendix dedicated to it.

3.3 Beam conditioning

3.3.1 Mechanical constraints within the wafer

Parameters of the wafer of silicon Having determined a target R of the radius of curvature for our silicon wafer, it is important to take into account whether the material can withstand the stress applied to curve it.
In order to study the deflection of the silicon wafer, the polychromatic can be considered as a fixed beam of Bernoulli, that is to say composed of plan sections remaining plan and perpendicular to the axis of the beam. The figure 27 represents a view of the wafer ans its characteristics, available on the site of Crystal GMBH, Germany and Hasby charts :

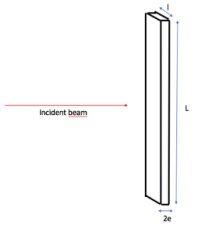

$$\left\{\begin{array}{ll} e = 5.0 \cdot 10^{-4}\text{m} & \text{half thickness of the wafer} \\ L = 1.0 \cdot 10^{-1}\text{m} & \text{Height of the wafer} \\ l = 1.0 \cdot 10^{-1}\text{m} & \text{width of the wafer} \\ E = 170Gpa & \text{Young's modulus} \\ G = 0.5\frac{E}{1+\nu} & \\ \nu = 0.42 & \text{Poisson's ratio} \\ \sigma_{max} = 80MPa & \text{The maximum admissible mechanical constraint} \end{array}\right\}$$

Figure 27: Characteristics of the wafer

Curvature of the wafer Given an isotropic material,it is possible to consider the stress as a function of y. I is the quadratic moment of the cross section and M the moment applied on it [**mecanique**]. In this case, $I = 1.04 \cdot 10^{-12}\text{m}^{-4}$.

As a reasonably accurate approximation, the torque M needed to bend the wafer to be applied on its extremity. Besides, in order to maintain the elasticity of the wafer while curving it, the wafer must remain in the domain in which :

$$\sigma(y) = E \cdot \frac{\Delta L(y)}{L} \tag{36}$$

The deduction $\frac{\Delta L}{L} = \frac{e}{R+e}$ is easy. As a consequence, the expression between the moment needed to curve the silicon wafer and the radius of the circle is :

$$M = \frac{E \cdot I}{R + e} \tag{37}$$

Thanks to the method presented in part 2.3, the radius of curvature and the momentum applied on the beam can be determined.

Verification of the constraint on the wafer The stress resulting from the torque M must never overcome the limit value of σ_{max} in order for the wafer not to shatter. That is to say M must satisfy to the equation 38. Both momentums for iodine and gadolinium respect this requirement.

$$\sigma_{max} > \frac{e}{2} \cdot \frac{M}{I} \tag{38}$$

3.3.2 Design of the crystal support system

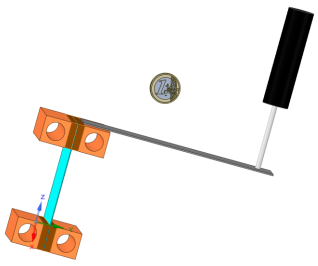

Figure 28: Schematics of the crystal support system designed on SpaceClaim;1 euro coin for scale

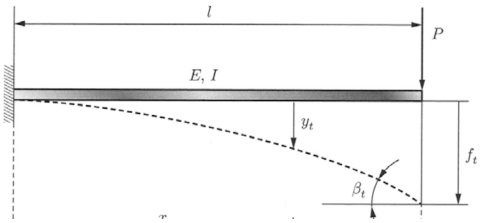

Figure 29: Schematics of a fixed beam [17]

Figure 30: Design of the crystal support system

In order to apply the required momentum at the top of the wafer (4.9×10^{-3}Nm as a reminder), the system presented on figure 28 will be used. A thin board (dark grey on figure 28), integral with the wafer on one of its ends, will be bent on its other end by a motor. The force applied by the motor can easily be computed, knowing that the effective length of the board is nine millimeters:

$$F = \frac{M_O(F)}{OM} \tag{39}$$

where O is a point at the top of the wafer and M is at the center of the contact between the motor on the board (respectively in light and dark grey on figure 28). Differentiating equation 37 gives the resolution the motor needs to have, knowing the maximum relative variation on the curvature of the wafer is 10^{-2}:

$$\delta F = \frac{E \cdot I}{OM} \frac{\delta R}{R^2} \tag{40}$$

Such force will be obtained by displacing the end of the board thanks to the motor. The displacement f can be approximated thanks to the following equation, taken from [17] :

$$f = F \frac{L^3}{3EI} \tag{41}$$

where L=OM. The final displacement is f $= 4 \cdot 10^{-4}$m for iodine and f $= 7 \cdot 10^{-4}$m for gadolinium. The required resolution is δf $= 1.5 \cdot 10^{-6}$m. Such precision can be obtained with a piezoelectric motor, represented in black and light grey on figure 28. Tekceleo company sells appropriate motors for instance (see [25]).

3.3.3 Thermal Dissipation

Crystal Cooling SystemThe crystal absorbs energy from two different sources :

- BeamLine : $Q = 29$mW from the two wavelength after the filter ;
- Radiative Flux : $Q_{rad} = S\epsilon\sigma(T_{wafer}^4 - T_0^4) \simeq 0.9$W from the enclosure ;

Amazingly, the main source of energy on the wafer comes from the radiative flux, initially neglected. Using the equations below, it results the couple (Q, R) that satisfy:

- $T_{surface} < 100K :=$ Maximum surface temperature to prevent burning
- $T_{average} \simeq 125K :=$ Avoid thermal deformation and stress due to load
- $Re < 2400 :=$ Laminar flow for the liquid nitrogen to reduce vibrations
- $R < R_{max} = 1cm :=$ Geometrical constraints of cooling system

The cooling agent chosen is liquid nitrogen at $77K$. It will flow in copper blocs carved and will evacuate heat on each extremity of the wafer as shown in figure (28). Indium/Gallium foil is used as contact pad, with excellent thermal conductivity to prevent bending or shatter of the wafer. Additionally, the study of the stationary regime allows to size the system given these assumptions :

- The whole setup is placed in vacuum, heat flux is therefore conserved through the three layers and none is lost via convection ;

– The heat flux is applied in the center of the crystal, symmetry applies ;

– Assuming the liquid nitrogen N_2 creates a liquid thermostat in the surrounding copper due to sufficient mass flow.

Given a circular cross section for the liquid nitrogen and a laminar flow to reduce vibrations, the flow of liquid Q must not exceed a maximum flow Q_{max} such as :

$$Re = \frac{\rho Q 2R}{\mu \Sigma} < 2400 \tag{42}$$

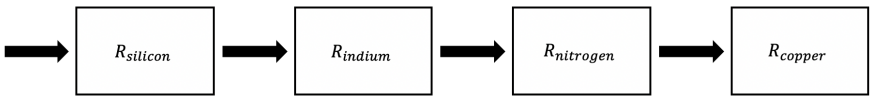

Figure 31: Thermal resistance system for the crystal cooling

Furthermore, with Fourrier's Law and the electric analogy, the global resistance of the system is obtained in figure (31). R_{copper} is deduced from the equivalent for burried objects as shown in []. Temperature difference is given by :

$$R_{copper} = \frac{\cosh^{-1} 2}{2\pi\lambda_{copper}} \tag{43}$$

$$R_{N_2} = \frac{1}{2\pi R * h(Nu_D)} \tag{44}$$

$$\Rightarrow \Delta T = \Phi \sum_i R_i \tag{45}$$

Given the laminar regime, Nusselt number Nu_D for a Prandt indice $Pr > 0.6$ gives :

$$Nu_D = 4.364 \longrightarrow h_\infty = \frac{\lambda Nu_D}{2R} \tag{46}$$

After solving the equations, a suitable solution is obtained for $R = 0.5cm$ and $Q = 10^{-3} L/s$. Final temperature on crystal at stable regime is $T_0 = 79$K.

Filter Cooling System The two slits have to be made included in a system that can dissipate a power of $\Phi = 764$W. As shown in figure (11), it will be made out of three pieces of copper of thickness e adjusted to let only two slits of 10µm each. The filter receives considerable amounts of power, hence the need to cool effectively the copper pieces. The sizing of the flow Q must satisfy two conditions :

– $T_{surface} < 30C$ to prevent dilatation ;

– $Re < 2400$ to ensure laminar flow ;

Water is used and flows within the carved tubes. Using the same reasoning as above, the resistances are calculated taking into account the thermal properties of the materials. There are two tubes with flowing nitrogen acting as resistances in parallel. The total resistance is deduced as follows :

$$R_{filter} = \frac{1}{2 \cdot (R_{copper} + R_{water})^{-}1} = \frac{R_{copper} + R_{water}}{2} = \frac{\Delta T}{\Phi} \tag{47}$$

After solving the equations, the thermal resistance obtained for both contrast agents is:

$$R_{filter} = 1.55 \cdot 10^{-3} \mathrm{KW}^{-1} \tag{48}$$

This leads to an augmentation of the temperature of 1.6K and a dilatation of the copper of 0.5µm, which represents 5% of the size of the slit. Regarding the wavelength, it is negligible.

3.3.4 Design of the support & adjustability

In this section will be given a global look on the system and precisions on the different parameters of the support.

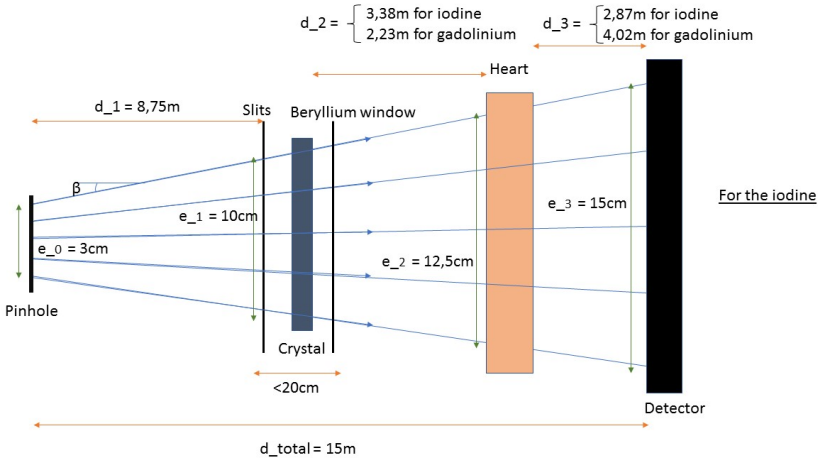

Figure 32: Above view of the beam conditioning device

The distances were calculated respecting two conditions :

- the monochromatic rays at λ_1 and λ_2 must cross in the heart
- those monochromatic rays must respect the detectors dimensions: about 15 cmlarge, vertical distance between the two monochromatic rays lower than 20cm. The two monochromatic beams must not be superposed on the detector. This will be summed up in the following scheme

After to the calculus given in appendix C, $d_{iodine} = 3.38\mathrm{m}$ and $d_{gadolinium} = 2.23\mathrm{m}$

3.3.5 Sizing of the enclosure

The interface between the vacuum chamber and the chair has to be designed so that the beamlights reach the patient's heart and resist the difference of pressure. To achieve that, a small window made out of beryllium will be placed between the crystal and the patient. Known for its transparency to X-rays and good mechanic resistance, beryllium is a good material.The energies of the beams are low enough to not take account of possible heating problem (energy around 50 keV). Therefore, there is no need to consider a cooling system for the beryllium window. However, the window has to endure the force that is created by the difference of pressure between the air and the vacuum inside, making 10^5 Pa
Therefore, the length a, the height b and the thickness e must verify $a \geqslant 10$ cm and $b \geqslant 6.4$ mm.
The constraint of he beryllium window has to be inferior to the constraint of maximum elasticity of the beryllium :

$$\sigma = \frac{M \times \frac{e}{2}}{I} \leqslant E_{beryllium} \tag{49}$$

Where M is the moment of the force created by the difference of pressure along, e, the thickness of the window, I the quadratic momentum of the window and E, the constraint of maximum elasticity of the beryllium. As a consequence,the minimum thickness of the window is 190 µm. The following dimensions fit the criteria of the problem.
Hence, $a = 12$ cm, $b = 1$ cm,$e = 250$ µm.

With these values, $\sigma = 138.2$ GPa $\leqslant E_{beryllium} = 240$ GPa.
And the transmittance of the window can be computed with the software XOP and the transmittance value obtained for this beryllium window at energy range between 10 and 50 keV is 99.998%. Finally, it is big enough to let the beams get outside of the vacuum chamber.

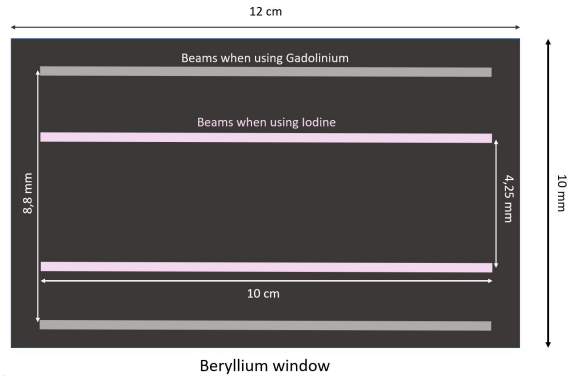

Figure 33: Dimensions of the beryllium window and of the different beams

3.4 Sample environment

3.4.1 Design of the chair

The chair is composed of two main parts : the upper part (the chair itself), that is able to move vertically and the motorized lower part (the support). To ensure stiffness and lightweight, the upper part of the chair will be crafted in aluminum. The lower part will be in steel, more resistant and durable. Both are linked thanks to a triangulated structure, ensuring the durability of the system and restricting vibrations. To be comfortable, memory foam cushions will be added on the top of the aluminum layout. The chair sit is 50 cm wide and 55 cm long, while the backrest is 70 cm high.
The chair also needs to fit any patient's morphology. In order to achieve that, adjustable armrests were designed, as well as an adjustable headrest and footrest. The patient can move them when he sits on the chair, but then during the scan the different rests are fixed.
As a matter of fact, the patient must not move when he is hit by the beam, so that the scan does not have to be repeated. Seat belts are therefore fixed on the chair in order to prevent the patient from moving. The chair must also be designed in a way that lets the beam go through it, that is why the backrest has a hole at the level of the patient's heart.

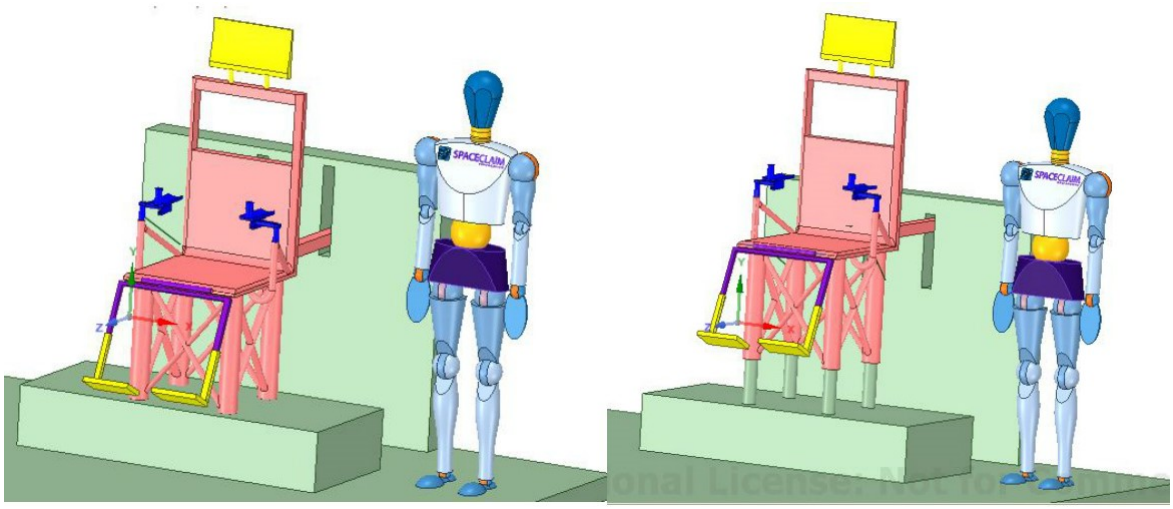

Figure 34: Model of the motorized chair : low position (left) and high position (right)

3.4.2 Modeling of the chair behaviour

The chair is motioned by a brushless motor. Indeed, this kind of motor has few energetic losses and wear. It also creates very few vibrations, especially compared to a classic DC motor, and obviously there must not be vibrations in the system to

avoid blurring the image. It can also be precisely piloted in term of speed response. The chosen motor is therefore the SGMGV brushless motor from Yaskawa®.
Then, the motor drives a gearbox which divides the revolving speed by 4. The rotation movement is then converted to a translation movement thanks to a ballscrew (attached to the shaft) and a nut (linked to the chair). This system has few pieces, which limits vibrations.

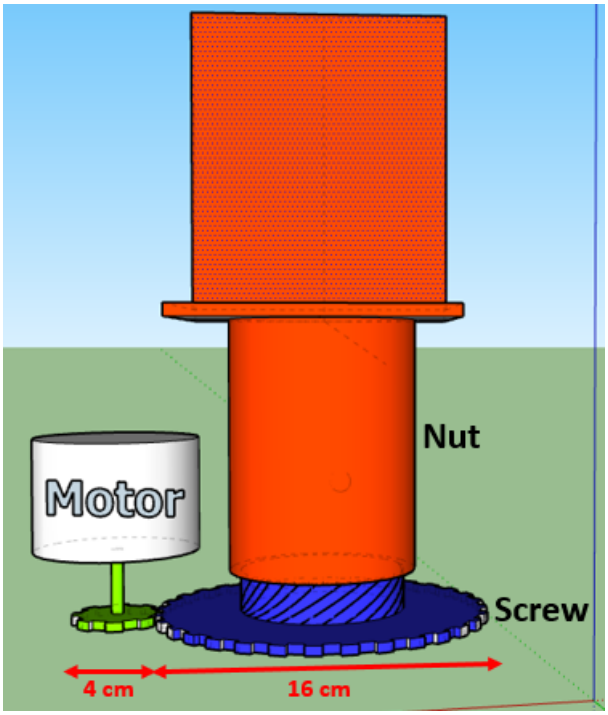

Figure 35: Kinematic schema

About the command, the following speed law has been found to have steady speed during the scan time and low acceleration before and after this time (less than an elevator one).

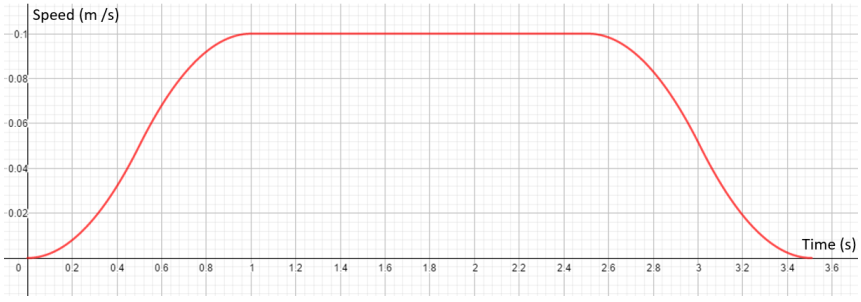

Figure 36: Speed command

A feedback control is set up in order to minimize the gap between the desired speed and the chair one. However, it is not enough to get a good answer speed, particularly

because of the resistant torque due to the weight of the patient and the chair. That is why a proportional integral corrector has been added. Thus, the following bloc diagram sums up well the desired behaviour for the system.
A simulation of the chair behaviour with the X-COS software gives a good speed response : the biggest gap between the command and the answer is 1.5 mm/s, which is during the acceleration period. For the time span with a steady speed, there is not any gap.

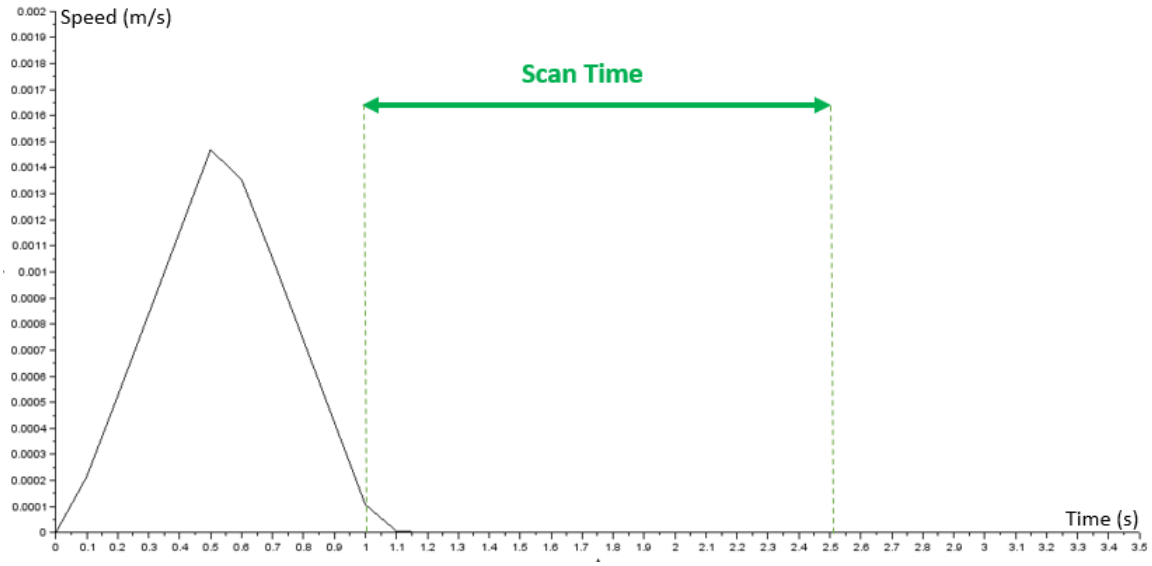

Figure 37: Gap between desired and answer speeds

3.4.3 Problem of vibrations

During the scan time span, the speed must stay steady, and every perturbation has to be overcome. In particular, the vibrations created by the rotation of the motor must not interfere with the heart scan. A way to limit these vibrations is to use a balanced motor, that is why a G1 motor type has been chosen according to the ISO 1940 norm. This kind of motor has its gravity center close to the inertia axis in order to keep the resistant torque under 100 $g \cdot mm$.
The structure of the chair itself also allows to reduce vibrations; indeed, it is made of aluminium and steel, whose frequency of resonance are above 40 Hz, which is the maximum steady rotation speed of the motor. The chair also rests on a triangulated structure, which makes it stiffer and limits the vibrations.

Part II
Evaluation of the solution

4 Results

4.1 Medical requirements

Using such technologies, the synchrotron X-ray angiography has to meet with several medical specifications. Those requirements are summed up in the following table. [18]

Max. radiation dose	200 mGy
Max. irradiated zone	15 cm
Max. number of images acquisition	5
Min. Signal to Noise Ratio of the contrast agent	5
Min. Image resolution	0.5 mm

Table 8: Physician requirements for the angiography

The following scheme clearly resumes globally the way the whole system works from the generation of the beam to the patient.

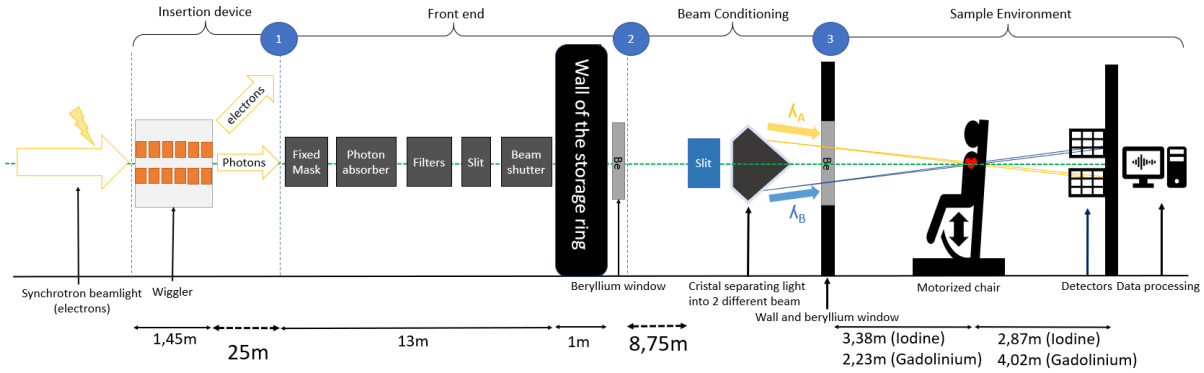

Figure 38: Global trajectory of the synchrotron beamline through the designed system

At each step, the beam gets through several devices that change its dimensions, flow, power and wavelengths. Until it gets to the monochromator, its spectrum is large and continuous, and then it is only composed of two wavelengths (which is why the flow is more complex to deduce from the power at the beginning). A certain amount of energy is absorbed at each step, willingly or not. The evolution of the beam can be followed by watching its characteristics at the end of each step.

Contrast agent	**Iodine**		**Beam dimensions**		**Gadolinium**	
Physical quantity	Outgoing flow ($ph.s^{-1}$)	Outgoing power (W)	Height (mm)	Width (mm)	Outgoing flow ($ph.s^{-1}$)	Outgoing power (W)
Insertion device		$1.8 \cdot 10^{4}$	5	100		$1.8 \cdot 10^{7}$
Front end		764	5	30		125
Beam conditioning	$1.74 \cdot 10^{11}$	$1.84 \cdot 10^{-3}$	0.01	100	$2.38 \cdot 10^{11}$	$3.8 \cdot 10^{-3}$
Sample environment (patient)	$1.65 \cdot 10^{11}$	$8.8 \cdot 10^{-4}$	10	120	$2.36 \cdot 10^{11}$	$1.9 \cdot 10^{-3}$
Sample environment (detector)	$3.88 \cdot 10^{9}$	$4.0 \cdot 10^{-5}$	10	150	$8.10 \cdot 10^{10}$	$6.4 \cdot 10^{-4}$

Table 9: Flow, power and dimensions of the beam at each step of the line

The absorbed dose of X-ray is $27.8mGy$ with iodine and $32.6mGy$ with gadolinium, which is significatively lower than the $200mGy$ limit, so the patient is safe, even after several images (the maximum number of 5 is reachable).
To obtain a SNR over 5 and thus a sufficient image quality, $3.36 \cdot 10^{-5}W$ were needed on the detector with iodine and $4.60 \cdot 10^{-4}W$ with gadolinium. So the constraint is respected but the values are closer to the minimum.

4.2 Usage protocol and security rules of the patient's environment

4.2.1 Protocol of the X-ray angiography

Here is the protocol of an angiography scan :

- The patient enters in the room and sits on a chair (the chair is placed at the low level at the beginning).
- The doctor adjusts armrests, headrests and footrests then adjusts the chest holds and the sit-belt.
- The doctor injects the contrast agent into the patient's arm.

– The doctor pushes the activation button, that he will have to hold until the end of the angiography. If he has a problem, the release of the button will trigger the emergency brake.

– The chair moves up to the high level.

– The doctor warns the patient to not move.

– Then the scan begins : the chair slowly comes down while the heart is scanned with X-rays.

– When the chair is again at the low level, if the image is judged as good by the doctor, the patient can leave the room. If not, another scan will be realized.

4.2.2 Emergency protocol

The emergency protocol starts if the doctor releases the pressure on the activation button (if he notices any problem) or in case of power shutdown.
The device is equipped with a braking system, including 2 types of brakes. The first one is the motor brake : the motor becomes a generator and decreases slowly its rotation speed. The kinetic energy is transformed into heat by Joule's effect in the resistor that is provided with the power supply of the motor and is located outside the building. This system allows to smoothly stop the chair even when a power cut occurs. The second system is a hand-brake for blocking the chair when it is not moving.
Another emergency device is a fast shutter. Its goal is to kill the beam if the chair is blocked. The delay of this intervention is about 3 ms. It prevents the patient from being burnt, especially if the chair's motor has a failure.

4.3 Calibration of the monochromator

4.3.1 General Results

Here is a global view of the angiography beamline's monochromator (figure 39), with the distances between each component :

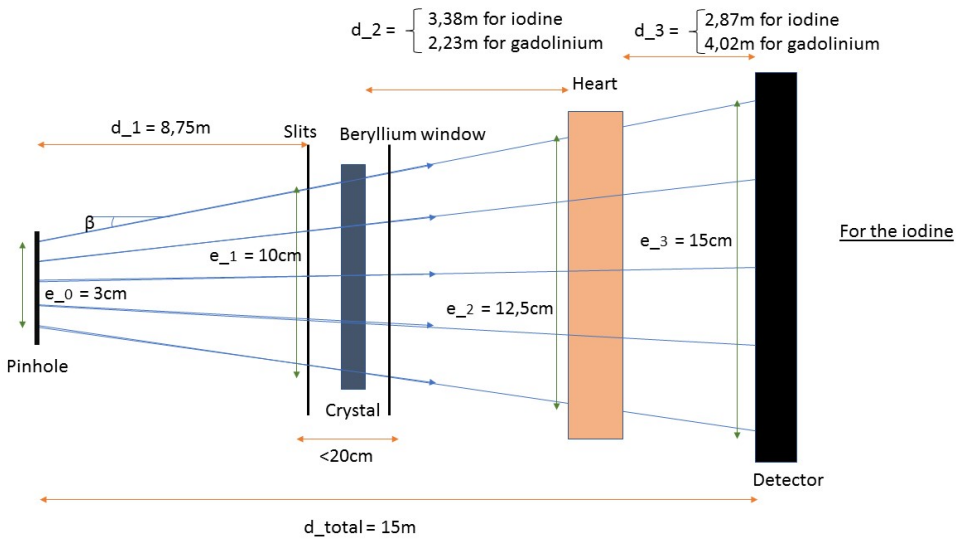

Figure 39: Above view of the beam conditioning device

This table gathers every informations on the chosen wavelengths.

Physical quantity	λ_{min}^{iodine}	λ_{max}^{iodine}	$\lambda_{min}^{gadolinium}$	$\lambda_{min}^{gadolinium}$
Wavelength	$3.73 \cdot 10^{-11}$m	$3.80 \cdot 10^{-11}$m	$2.38 \cdot 10^{-11}$m	$2.57 \cdot 10^{-11}$m
Energy	$3.33 \cdot 10^{4}$eV	$3.27 \cdot 10^{4}$eV	$52.2 \cdot 10^{4}$eV	$48.2 \cdot 10^{4}$eV
$\frac{\Delta\lambda}{\lambda}$	$1.64 \cdot 10^{-5}$	$1.61 \cdot 10^{-5}$	$8.07 \cdot 10^{-5}$	$7.45 \cdot 10^{-5}$

The following table gathers the main results regarding the photon flow going through the monochromator and being regulated by it.

Physical quantity	Symbol	Iodine	Gadolinium
Power incoming pinhole	$P_{pinhole}$	764W	125W
Slit Incident flow for ΔE	$\Phi_{slitsin}$	$7.65 \cdot 10^{13} ph \cdot s^{-1}$	$1.02 \cdot 10^{14} ph \cdot s^{-1}$
Slit Outgoing flow for ΔE	$\Phi_{slitsout}$	$9.00 \cdot 10^{10} ph \cdot s^{-1}$	$1.20 \cdot 10^{11} ph \cdot s^{-1}$
Wafer Outgoing flow for ΔE	$\Phi_{waferout}$	$8.71 \cdot 10^{10} ph \cdot s^{-1}$	$1.19 \cdot 10^{11} ph \cdot s^{-1}$
Outgoing power	$P_{outgoing}$	0.92mW	1.9mW

Here are described the geometric dimensions of the beam.

Physical Quantity	height	width
Beam 1m after the pinhole	5mm	3cm
Beam incident on the filter	8.5mm	10cm
Beam going out of the crystal	10µm	10cm
Beam going through the patient	1.2mm	12.5cm
Beam at the detector	2.5mm	15cm

4.3.2 Silicon Crystal Set-Up

The curved crystal is major component of the chromator, as it is the one diffracting the two monochromatic beams. The one used in this line is a wafer of silicon, available on the e-commerce site of Crystal GMBH, Germany.

Physical Quantity	Symbol	Iodine	Gadolinium
Dimensions	$L \cdot l \cdot e$	$10cm \cdot 10cm \cdot 1mm$	$10cm \cdot 10cm \cdot 1mm$
Radius of curvature	R	6.73 m	5.0 m
Momentum	M	2,1 $\cdot 10^{-1}$m	4,0 $\cdot 10^{-2}$m
Displacement	Δ_z	$5 \cdot 10^{-4}$m	$7.5 \cdot 10^{-4}$m
Incoming Beam Power	Φ_{in}	0.89W	0.15W
Beam power absorbed	Φ_{abs}	29mW	$0,6$mW
Radiative flux	Φ_{rad}	0.915W	0.915mW
Total Power Absorbed	$\Phi_{absorbed}$	0.94W	0.915W
Nitrogen Flow	Q_{N_2}	0.05 L/s	$0.05L/s$
Thermal Resistance	R_{tot}	7.18Ω	7.18Ω
Wafer Temperature	T_0	$78.7K$	$78.6K$

4.3.3 Filter Set-Up

Thanks to the filter which absorbs a certain amount of energy of the beam issued from the pinhole, the wavelenghts can be properly obtained. The table below gathers the information about this component.

Physical quantity	Symbol	Iodine	Gadolinium
Slits width	ϵ	10 µm	10µm
Beam Power Absorbed	Φ_{filter}	764 W	125 W
Nitrogen Flow	Q	0,5 L/s	0.5 L/s
Surface Temperature	T_0		
Thermal Resistance	R_{filter}	$1.55 \cdot 10^{-3}$KW^{-1}	$1.55 \cdot 10^{-3}$KW^{-1}
Filter Temperature	T_0	$21.6K$	$21.6K$
Dilation of Filter	$\Delta\epsilon$	0.5µm	0.5µm
Dimension	$L \cdot H \cdot W$	$20 \cdot 6 \cdot 4$ cm	20x6x4 cm

4.3.4 Enclosure Dimension

The enclosure between the vacuum chamber and the medical office has to be designed to that the beams reach the patients and resists to the difference of pressure applied on it. Here is a sum up of its features :

Physical quantity	Symbol	Iodine	Gadolinium
Dimensions	$a \cdot b \cdot c$	12 cm $\cdot$ 1cm $\cdot$ 250µm	12 cm $\cdot$ 1cm $\cdot$ 250µm
Transparency		99.8	99.8

4.4 Servicing, installation and security specifications of the Front-End

The Front-End major role is to prevent the Synchrotron of being polluted by any foreign body, such as air molecules in case of an accidental leak. Without the front-end system, such accident could create a plasma in the synchrotron, which could burn every composant and force to stop the synchrotron for a few months. As a consequence, the installation of the security components (such as the absorber, the fast shutter, the UHV valve, the ADL, the beam shutter and the beryllium window) should be made with extreme precautions.

Moreover, should a failure happen, the entire system should be checked before re-using the beamline. The fast shutter will also have to be changed if it had to sustain the beam, even for a short time.

As for the filters, the two sets can be switched depending of the contract agent needed for the patient (Iodine or Gadolinium). Both layouts are present at the same time in the UHV tube, and a system can lower or rise the filters so that the beam go through the right ones, at the demand of the doctor.

4.5 Servicing, installation and security specifications of the Insertion Device

Very strong forces are involved in a wiggler. Thus, in case of malfunctioning, it is crucial to adopt security systems to avoid catastrophes along the storage ring. In fact, if the jaws get in contact with the vacuum chamber, they would impose a very high mechanical load. If the vacuum chamber is broken and some air enters in the storage ring, the synchrotron would stop functioning for at least 6 months.

Firstly, in case of a motor's malfunctioning, in order to prevent the jaws from hurting with the vacuum chamber, four wedges are attached to the frame as shown in Fig.40. This system is called "Hard Safety" .
The second security system is constituted by triggers placed next to the jaws. When the jaws get closer than a certain safety distance ($1,3mm$ from the vacuum chamber), the triggers are pulled. Afterwards, the motor is shut down and the safety brakes are activated in order to stop the translations of the jaws.

Finally, a "Soft safety" is also adopted: if the user tries to impose a gap smaller than a safety distance between the jaws, the drive software delivered by Bonfiglioli® would refuse their demand.

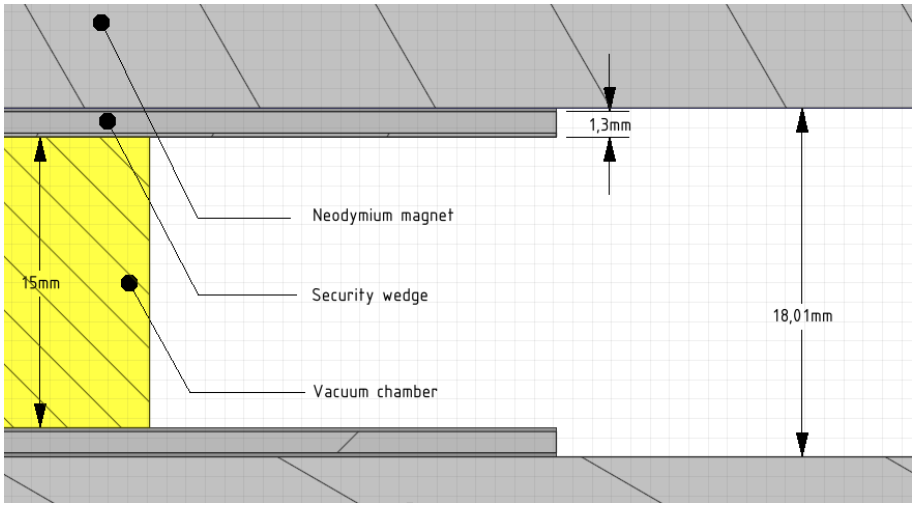

Figure 40: Security wedge.

5 Limitations and opportunities for improvements

5.1 Insertion Device

5.1.1 Electrons trajectory

As discussed before, the trajectory of electrons in wiggler is crucial. It must be a perfect sine inside the device and it has to be perfectly centered at each extremity. The magnet network used fits theoretically the requirements but the presence of inhomogeneities of the permanent magnets, pole imperfections and mechanical errors, must be taken into account as they introduce a certain level of imprecision. First, in order to correct the magnetic field quality inside the device, the shimming technique is adopted. Thin magnets (50µmto 100µm) are added on the neodymium magnets to adjusts the imperfect wiggler field and closely approximate it to an ideal sinusoidal field. According to the article [11] calculations have shown that the rms variation of the half-period field integrals should not exceed 0.1 to 0.3%, while the typical field-error achieved in hybrids is around 0.7%. The shimming technique is able to fully correct kick errors. Then to correct the magnetic field at each extremity to avoid electron loss due to their deviation, there are electromagnets at each extremity of the wiggler. The electromagnets are creating a precise controlled magnetic field to correct the exit trajectory of electrons. Since it is a weak magnetic magnitude, it does not heat up other components.

5.1.2 Jaws thickness

The magnetic field should stay constant over the perpendicular plan to the electron beam plan. Consequently, jaws and magnets must be sufficiently thick to neglect edge effects. Theoretically, the thickness should be ten times larger than the gap value [16]. In the wiggler, the gap value is 18mm, so jaws and magnets are 18 cm

width, which is very thick. In practice, for economic reasons, wigglerâs magnets are between 5cm and 10cm. Indeed, by measuring the magnetic field, it is possible to reduce jaws thickness as long as magnetic field remains constant around the vacuum chamber[16]. Thus, by reducing jaws and magnet thickness, it reduces the magnetic force upon the structure and it would be possible to reduce height and to use aluminum jaws instead of iron ones which are three times lighter and cheaper.

5.1.3 Go further...

Finally, it is important to remark that it is not a definitive solution. This work does not mention costs, uncertainties and a lot of technical and theoretical complex details. It could have been more precise and complete. Thus, it is highly recommended to improve the theoretical and technical understanding for the effective manufacturing of an insertion device.

5.2 Front-End

5.2.1 Thermodynamic models

The thermodynamic models used are very simple and the cooling of the components would require further calculation in order to be able to determine precisely the thermal flux that extracted from the component through water-cooling. To get a more precise estimation, a 2D model was made on the Freefem++ software (see figure 41. The results found seem to indicate that the cooling system was enough. However, a 3D calculation would allow to see the entire field of temperature to check for potential points with very high temperature.

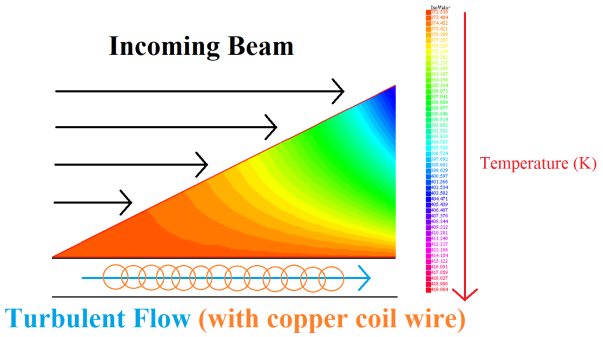

Figure 41: Numerical simulation on a horizontal slice of the "fixed mask" - Lower Half

5.2.2 Filters layout

In order to adapt the entering photon flux to the desired one, filters were designed and sized. The necessary thickness of each material is divided in the layers depicted

in the Figure 42, to be cooled in a likely way.

Iodine

Layer number	Material	Thickness (mm)	Absorption (W)
1	Graphite	0,1	500
2	Graphite	0,3	400
3	Graphite	0,6	500
4	Aluminum	0,1	400
5	Aluminum	0,2	400
6	Aluminum	0,3	500

Galodinium

Layer number	Material	Thickness (mm)	Absorption (W)
1	Graphite	0,4	900
2	Graphite	1,8	1050
3	Graphite	3,8	1150
4	Graphite	7	1250
5	Graphite	12	1200
6	Graphite	10	550
7	Aluminum	4	300

Figure 42: Filters layout for Iodine and Gadolinium

As it can be seen, the flux absorbed by each layer is not equal, hence not optimal. A possible improvement would be to size each layer of the same material in a more optimized way so that each sheet absorbs the same amount of power and to design the cooling system homogeneously.

5.2.3 Approximating the power density as homogeneous

Aiming to estimate the power absorbed through the pinholes, some approximations were made in order to enable the use of simple models, such as the consideration of a homogeneous power density. To obtain more precise results, the use of a adequate software – as SPECTRA – would be expected.

5.3 Beam Conditioning

5.3.1 Optical considerations

Throughout the report, assumptions are made on the optical features of the silicon wafer. On the one hand, they are not sensible to the temperature's augmentation of the wafer : the cooling system is supposed to evacuate all the heat provoked by the beam. On the other hand, the crystal is supposed to have a perfect crystalline structure which is almost impossible to get on a wafer of theses dimensions. The defaults of the structure would therefore trigger aberrations on the diffracted beams. Likewise, the surface of all optic devices has been assumed perfect. The inevitable imperfections are another source of aberrations.

5.3.2 Mechanical considerations

There is room for improvement in the mechanical system used to curve the crystal. Indeed, if it is clear that a piezoelectric motor can be used to achieve such an end, the precise system which converts the rotation of the motor into the required translation was not precisely described. A possible solution could include an endless screw and a reducer.

The mechanical study that was conducted also resorted to a few approximations; for instance, the crystal was assimilated to a perfect Bernoulli beam, and the geometry of the board used to curve the crystal was simplified. A more thorough study could try and refine the mechanical study as a whole.

5.3.3 Thermal considerations

Considering the monochromator and the filter placed just before it, there is room for improvement. Indeed, both those elements are placed close to each other (about 10cm) while they are refrigerated to very different temperatures. Indeed, the copper filter is refrigerated by water at a temperature of $20C$ while the silicon crystal is maintained at $80K$ thanks to nitrogen. Consequently, those elements share heat flows and lead to an important loss of energy. This could be improved by using materials functioning at closer temperatures.

It could perhaps also be possible to design a solution with only one cooling system, which would simplify the monochromator as a whole.

All thermal calculations have been realized in steady thermal regime. To be more precise, they could be recomputed in unsteady regime.

5.3.4 Geometric considerations

The monochromator allows for the creation of two monochromatic beam lights after the silicon crystal. However, the two beams are physically very close to each other, which means not a lot of margin for error.

5.4 Sample Environment

5.4.1 Image processing

As seen before, the heart is beating during the scan time which means it is moving and swelling. Thus, each line of pixels of the picture is shifted with its own scale. The produced image has to be numerically treated. However, the time is missing to create an algorithm which allows to shifts and adapt the scale of each line in order to recompose veins of the heart. But, this kind of algorithm does exist. It allows to get a recomposed picture, faithful to the reality of the heart. Moreover, as up to

5 images of the heart can be obtained, an advanced algorithm could benefit from different points of view to recreate a clean image.

5.4.2 Difficulty to respect the constraints

Even if it is currently possible to respect all the constraints, it would be interesting to get as close as possible to the maximum number of photons allowed to get the best image quality possible. It is quite complex because each change in the requirements in terms of power, flow or wavelengths implies several changes in the previous parts of the synchrotron line to adapt. Even changing from iodine to gadolinium requires to move the chair in the room. To get closer pairs of wavelengths or more control over the photon flow, an important precision is needed at each step.

Conclusion

This report provides the main elements for the conception of a synchrotron beamline dedicated to the achievement of a coronarian angiography. A synchrotron beamline is a very complex system, involving a wide range of physical issues, from mechanics to thermics through optics. The engineering team has to tackle every single part of an almost 50 meter long line while keeping a general view in order to meet the physicians requirements.

Given a further review of the problem, this document can be used as a basis for the actual construction of the beamline.

Acknowledgements

The beamline design team would like to thank cheerfully the experts and researchers who dedicated part of their time to our project : Pr. François Bertrand, Dr. Yves Dabin, Dr. Thierry Moreno, Dr. Oliver Marcouillé and, of course, Dr. Sunao Takahashi for their priceless help in the conception of the line. We gratefully thank Pr. Pascal Morenton, Pr. Pierre-Eymeric Janolin, Pr. Pascal Bernard and Dr. Gabriel Stancu for their precious support all along the week and more generally for the organization of this course.

References

[1] Dr. Takahashi, SPring-8 synchrotron, *Private communication.*

[2] Consulted on the 24th of January 2019. "http://www.esrf.eu/UsersAndScience/Publications/Highlights/2005/XRS/XRS6". In: ().

[3] Felicie Albert. "Rayonnement synchrotron base sur l'interaction laser-plasma en regime relativiste". In: (Dec. 2007).

[4] ANSM. "CLARISCAN 0,5 mmol/mL, solution injectable". http://base-donnees-publique.medicaments.gouv.fr/affichageDoc.php?specid=61696661&typedoc=R. 2017.

[5] ANSM. "IOMERON 400 (400 mg d'Iode/mL), solution injectable". http://base-donnees-publique.medicaments.gouv.fr/affichageDoc.php?specid=60495132&typedoc=R. 2017.

[6] Hideki Aoyagi et al. "Alignment of photon beamline components of the SPring-8 front end". In: (2002), pp. 280–287.

[7] G. Brown et al. "Wiggler and undulator magnets â A review". http://www.sciencedirect.com/science/article/pii/0167508783911055. "Nuclear Instruments and Methods in Physics Research". 1983.

[8] Henrik Buhr et al. "Measurement of the mass energy-absorption coefficient of air for x-rays in the range from 3 to 60 keV". In: Physics in Medicine & Biology 57.24 (2012), p. 8231.

[9] Tonio Buonassisi. "Bragg's law". https://ocw.mit.edu/courses/mechanical-engineering/2-627-fundamentals-of-photovoltaics-fall-2013/lecture-videos-slides/MIT2_627F13_lec03.pdf. 2011.

[10] FraneÌ§ois Estève et al. "Coronary angiography with synchrotron X-ray source on pigs after iodine or gadolinium intravenous injection". In: Academic radiology 9.1 (2002), S92–S97.

[11] S.C. Gottschalk et al. "Wiggler error reduction through shim tuning". "Nuclear Instruments and Methods in Physics Research Section A: Accelerators, Spectrometers, Detectors and Associated Equipment". 1990.

[12] Renevier H. "Introduction au Rayonnement Synchrotron". In: Grenoble INP phelma 5.3 (1998), pp. 606–608.

[13] JÃ$\frac{1}{4}$rgen HÃrtwig. "Optique of visible light and X-rays optic, a basic introduction". In: ESRF (2004).

[14] M.O. Krause and J.H. Oliver. "X-ray Properties of the Elements". http://henke.lbl.gov/optical_constants/pert_form.html. 1979.

[15] H. G. Lee et al. "Analysis and Design of Backing Beam for Multipole Wiggler(MPW14) at PLS". In: (May 2005), pp. 3940–3942. ISSN: 1944-4680. DOI: 10.1109/PAC.2005.1591676.

[16] Dr. Marcouille. "SOLEIL Synchrotron, private communication". In: ().

[17] Thomas Gmur John Botsis Michel Del Pedro. “Introduction a la mecanique des solides et des structures”. In: (2012). 3eme edition PPUR.

[18] Irène NENNER, Jean DOUCET, and Hervé DEXPERT. “Rayonnement synchrotron et applications”. In: Techniques de l’ingénieur. Analyse et caractérisation 4.P2700 (1996), P2700–1.

[19] J. Rauss R. Jean. “Sur la protection contre les entrées d’air dans les installations sous vide”. In: Le Vide 111 (1964), pp. 123–127.

[20] Guillaume Reinhart et al. “Formation dynamics of solidification microstructures of metallic alloys: characterisation by synchrotron X-ray imaging”. In: (Oct. 2006).

[21] I Ching Sheng et al. “High Heat Load Components in TPS Front Ends”. In: Proceedings of EPAC08, Genoa, Italy (2008).

[22] Yunn-Fang Song et al. “Study of the transit time of pressure propagation in an acoustic delay line”. In: Review of Scientific Instruments 57.12 (1986), pp. 3063–3065.

[23] U.S. National Bureau of Standards. “Photon cross sections, attenuation coefficients and energy absorption coefficients from 10 keV to 100 Gev”. In: https://www.govinfo.gov/content/pkg/GOVPUB-C13-/pdf/GOVPUB-C13-.pdf (1969).

[24] Toshio Takiya, Tetsuro Mochizuki, and Hideo Kitamura. “Development of enhanced heat transfer coolant channels for the spring-8 front end components”. In: Spring-8 Annual Report (1998), pp. 164–166.

[25] France Tekceleo. “Motorisations piezoélectriques avec capteurs intégrés”. http://www.tekceleo.fr/wp-content/uploads/2018/12/FICHE-WAVELLING-2018.pdf. 2019.

[26] M Tischer, J Pflger, and W Decking. “A Permanent Magnet Wiggler Design for the TESLA Damping Ring”. In: (Feb. 2001).

[27] K. Wille. “Introduction to insertion devices”. In: ().